Received: 1 December 2021 | Revised: 9 June 2022 | Accepted: 12 June 2022

DOI: 10.1002/dep2.200

The Depositional Record
Open Access
A journal of the International Association of Sedimentologists
WILEY

ORIGINAL ARTICLE

Microbial EPS-mediated amorphous calcium carbonate–monohydrocalcite–calcite transformations during early tufa deposition

Paul L. Broughton

Broughton and Associates, Calgary, Alberta, Canada

Correspondence
Paul L. Broughton, Broughton and Associates, PO Box 6976, Calgary, Alberta, Canada.
Email: broughton@shawcable.com

Abstract

The Holocene Wolfenden tufa deposit in south-eastern British Columbia, western Canada, preserves a unique record of the earliest stages of calcium carbonate deposition resulting from microbial extracellular polymeric substances-mediated precipitation of amorphous calcium carbonate (ACC) with partial transformation to monohydrocalcite (MHC) and subsequently to nanocrystalline calcite. This is the first documentation of tufa mineralogy involving ACC transformation to MHC. Progressive dehydration triggered ACC–MHC–nanocrystalline calcite transformations on bryophytes, algae and cyanobacteria sheaths. The adsorption of extracellular polymeric substances matrix molecules into the ACC and ACC–MHC structures preserved polymorph mineralogy of incomplete transformation. Unusual concentrations of biofilm extracellular polymeric substances filaments provided nucleation sites for the ACC precipitation. The ACC nucleation calcified extracellular polymeric substances filaments and resulted in partially coalesced arrays of nanoscale ACC spheroids. Mesocrystalline structures of MHC reconfigured the concentric growth layers of ACC precipitate with bulbous ACC–MHC protuberances. Nanocrystalline rhombic faces of calcite developed within and on the surfaces of the ACC–MHC protuberances. Dehydration of these concentric growth layers of ACC–MHC resulted in the transformation into nanocrystalline calcite with substrates coalesced into micrite fabrics. Recrystallisation obliterated evidence of the calcified extracellular polymeric substances filaments and resulted in microcrystalline calcite spar domains as the widespread encrustation fabric. Localised magnesium adsorption during nucleation of the ACC within the biofilms resulted in needle calcite crystals without the precursor ACC–MHC transformation process. Microbial extracellular polymeric substances-mediated precipitation of ACC as a necessarily critical step in the earliest phase of the tufa deposition process, leading to the nucleation of calcite has been underappreciated and generally not considered. These earliest stages of calcium carbonate precipitation are proposed as a possible template for other tufa deposits, where the evidence of microbial extracellular polymeric substances-mediated precipitation

of ACC with transformation to MHC and subsequently to nanocrystalline calcite has been obscured by recrystallisation into micrite and spar fabrics.

KEYWORDS

amorphous calcium carbonate precipitate, calcium carbonate polymorph transformation, EPS, monohydrocalcite, Wolfenden tufa

1 | INTRODUCTION

The Wolfenden tufa, a 2000-year-old deposit in south-east British Columbia, is located along the Rocky Mountain Trench in the eastern Canadian Cordillera (Figure 1). Research into the morphogenesis of the Wolfenden tufa fabrics indicates that the widespread precipitation of amorphous calcium carbonate (ACC) also resulted in sequences of ACC—monohydrocalcite (MHC)—nanocrystalline calcite (CC) polymorph transformations, observations not previously recorded for tufa depositional processes. This deposit provides new insights into microbial controls on the earliest stage of calcium carbonate precipitation known to date for the deposition of cold water tufa. This research documents a tufa depositional process with a precursor mineralogy resulting from microbial EPS-mediated nucleation of ACC, followed by transformation to MHC and subsequently CC. Evidence for this process is uniquely preserved in the Wolfenden tufa, in contrast to the widely observed direct transformation in other tufa deposits of unstable ACC to stable CC without evidence preserved of the intermediate semi-stable polymorphs such as MHC or vaterite. Evidence for these earliest stage by polymorph transformations may have been obliterated elsewhere. The unique preservation at the Wolfenden tufa may be a depositional template for possible application to other cold water tufa deposits.

Observations of ACC are rare in non-marine calcium carbonate deposits (Jones & Peng, 2012; Obst et al., 2009; Peng & Jones, 2013; Swainson, 2008). There have also been a few records of ACC as a precursor polymorph to the nucleation of CC, particularly associated with hot spring tufa deposits (Jones & Peng, 2012) or in cooler water tufa deposits (Rainey & Jones, 2010). The rarity of ACC observations associated with naturally occurring tufa calcite is also related to the age of such deposits since

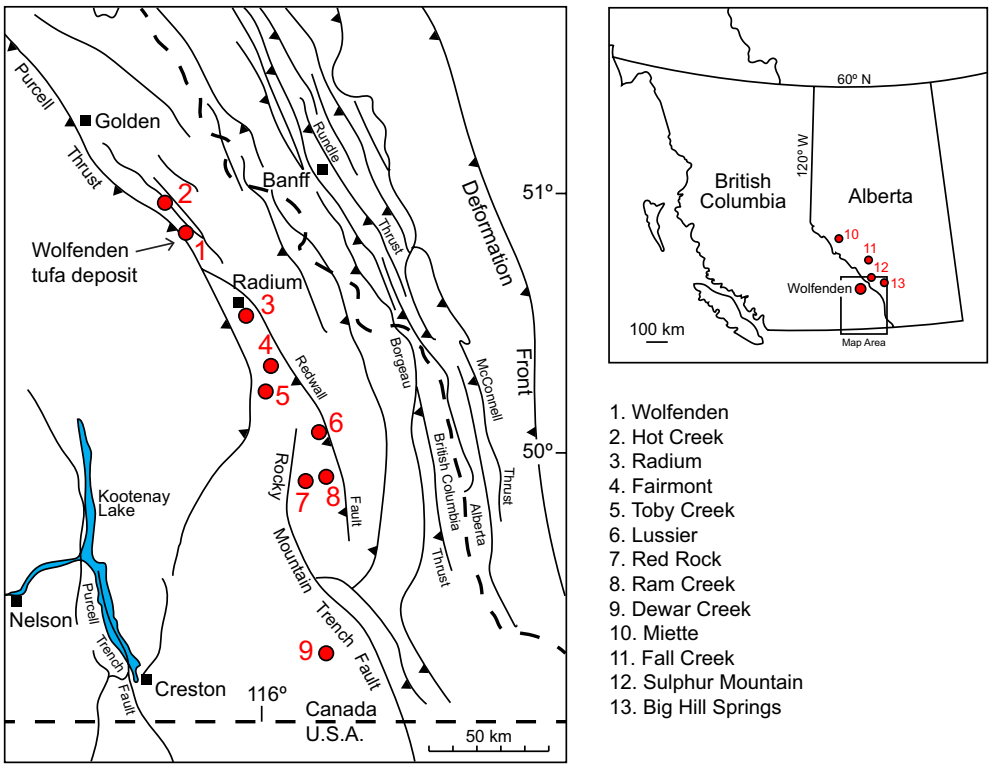

FIGURE 1 The distribution of tufa deposits along the Rocky Mountain trench in south-eastern British Columbia and major thrust and extension faults. Modified from Gabrielse (1991) and Grasby and Hutcheon (2001).

ACC is inherently unstable in ancient (pre-Pleistocene) rocks as are kinetically metastable vaterite and MHC. In contrast, the formation of ACC with transformation to aragonite by marine organisms is widely documented (Mass et al., 2017; Politi et al., 2004; Weiner et al., 2003). Experimental preparations of synthetic calcite also confirm that precipitation of a precursor ACC may be involved in the nucleation process (Bots et al., 2012; Loste et al., 2003).

Tufa deposits provide insight to the mechanisms and extent that precipitation of unstable non-marine ACC transforms into more stable crystalline polymorphs. Dehydration of an unstable ACC hydrated molecular structure results in the transformation to a more stable intermediate polymorph stage such as MHC (Kimura & Koga, 2011; Wang et al., 2015) or vaterite (Konrad et al., 2018; Rodriguez-Blanco et al., 2011; Rodriguez-Navarro et al., 2007). These minerals may be stabilised with the adsorption of ions and subsequently transformed by solid state solution to stable nanoscale crystalline calcite (CC). There is recognition that microbial EPS-mediated ACC precipitate can be stabilised in its hydrated form by the adsorption of organic compounds or metallic ions (Deng et al., 2015).

Microbial processes exert controls on calcite nucleation sites and are recognised as involving production of biofilm compounds such as EPS. These biofilm compounds have critical roles in the earliest stage of calcium carbonate (ACC) nucleation in cold water tufa (Jones & Renaut, 2010) and hot spring deposits (Jones & Peng, 2012). The biofilm EPS matrix provides substrate nucleation sites for ACC precipitate and the adsorption of organic compounds into the calcium carbonate molecular structure. This facilitates various levels of molecular stability and partially control the polymorph mineralogy and crystalline habits (Dupraz et al., 2004, 2009). This EPS-mediated process offsets issues related to lesser saturation levels of dissolved solids as precursors for calcium carbonate precipitation.

There is increasing research interest into precursor mineral precipitates such as ACC in tufa and travertine (Dupraz et al., 2009), albeit other intermediate polymorphs such as MHC have received little attention. These new insights are gradually replacing older models that calcite directly precipitated from bicarbonate solute in cold spring waters. There is also a growing recognition that the precipitation of ACC often occurs in non-marine thermal systems such as hot spring deposits of tufa and travertine (Peng & Jones, 2013), but also without evidence for other transitory polymorphs following the nucleation of ACC. This research presents the first documentation of MHC in tufa as an intermediary transformation mineral resulting from the dehydration of ACC. It is not known to what extent this ACC transformation sequencing in tufa may have involved vaterite or ikaite as an alternative polymorph, if at all. MHC, not vaterite, has been recorded in all tested specimens of the Wolfenden tufa. Nonetheless, ACC-vaterite in lieu of ACC-MHC may have been an ACC transformation process in other tufa deposits (Nehrke & Cappellen, 2006; Shen et al., 2006).

The extent to which all tufa depositional processes may have included precursor polymorphs, including ACC precipitate remains uncertain. The transformation of ACC to MHC before the transformation to calcite as a step in the dehydration process has not been previously recognised in tufa because research on these ultra-fabrics has been largely overlooked as the resolution limit of scanning electron microscopy (SEM) imaging is approached. The detection of ACC is limited by its nanodimensions, but also because it is a transient compound. It is thermodynamically and kinetically unstable under ambient conditions when chemically pure (Addadi et al., 2003; Albéric et al., 2018). The ACC transformations into metastable polymorphs with increased crystalline ordering may have been universal in tufa deposits elsewhere, but overlooked because evidence for the process was masked or obliterated by recrystallisation. This paper provides insight to the extent there is observable evidence that the earliest stage of the calcium carbonate precipitation in tufa involved the formation of ACC, followed by the transformation to MHC, and subsequently to CC.

1.1 | Terminology of mineral precipitation processes

There is a generalisation that the term travertine is to be used for deposits resulting from thermal waters and tufa terminology for ambient cold water deposits because these differing depositional conditions result in contrasting petrofabrics (Jones & Renaut, 2010; Pedley, 1990). Tufa deposits are broadly recognised products of calcium carbonate precipitation from mostly biotic-triggered precipitation (Chafetz & Folk, 1984). Travertine deposits are often generalised as semi-stratified accumulations characterised by markedly lower porosities with overall lesser levels of floral debris in contrast to tufa deposits with abundant floral debris (Gandin & Capezzuoli, 2008; Pedley, 1990). Tufa deposits characteristically developed on terrains with abundant floral debris, resulting in mouldic porosity levels of 20%–60% compared to relatively low levels of porosity in travertine deposits (Bonny & Jones, 2003a, 2003b; Gandin & Capezzuoli, 2008). Use of travertine terminology may imply that the precipitation of calcium carbonate occurred when thermal waters, supersaturated with calcium bicarbonate, responded to rapid and voluminous CO_2 degassing.

Carbonate precipitates in thermal springs are usually mixtures of biotic and abiotic processes (Capezzuoli et al., 2014; Rainey & Jones, 2009). In contrast, cold water tufa deposits are invariably dominated by extensive usage of biogenic processes (Rainey, 2009; Rainey & Jones, 2007). Tufa depositions were more responsive to cooler water chemistry and characterised by lower levels of solutes that require microbial mediation to trigger precipitation of calcium carbonate at ambient temperatures. Microbial EPS-mediated processes of tufa deposits do not necessarily require oversaturated water or degassing to trigger carbonate precipitation. Unlike travertine, aragonite is generally absent in tufa fabrics unless this mineralogy has resulted from an influx of spring water with high Mg/Ca ratios (Owen et al., 2010). Precipitation of travertine calcite is widely accepted as having resulted from rapid CO_2 degassing responsive to shifts in the supersaturation levels (Capezzuoli et al., 2014). Nonetheless, there is increasing recognition of microbial-mediated minerals precipitates in thermal springs (Fouke, 2011).

The EPS-mediated process contrasts with other models that suggest shifts in pH resulted in nucleation of calcium carbonate associated with EPS-laden biofilms with or without direct involvement of the microbes (Emeis et al., 1987; Knorre & Krumbein, 2000). It is a distinction between mineral precipitation within or on the microbe cell wall in contrast with nucleation sites on organic molecules of the EPS matrix produced by the microbe biofilm. Microbial films in tufa deposits often produce an extensive acid polysaccharide matrix, providing a substrate of nucleation sites for nanoscale mineral deposition. This contrasts with the biomineral process, sensu stricto, resulting from the metabolic activity within a microbe cell, such as during sulphate reduction or photosynthesis (Della Porta et al., 2022; Konhauser, 1997, 1998; Konhauser et al., 1993; Reitner et al., 1997). Biomineralisation is common in marine organisms by which they produce minerals, particularly aragonite, for the hardening of existing tissue. The biomineralisation process is utilised by diverse biological systems to produce various nanostructured mineralised structures found in nature and within certain viruses and unicellular organisms including bacteria, algae and fungi (Qin et al., 2020; Riding, 2000).

2 | GEOLOGICAL SETTING

The Canadian Cordillera developed during the Jurassic to Tertiary as island arc terrains collided against the western margin of North America. Successive deformation belts advanced eastward across modern day British Columbia and into western Alberta (Coney et al., 1980; Fulton, 1971). Compression deformation ended in the southern Cordillera during the Eocene as deep-seated extensional faults developed in the south-eastern Cordillera concurrent with westward plutonism and volcanism. Regional right-lateral strike-slip fault movements have been intermittent since the Eocene. A regional fault system evolved as the 1600 km long Rocky Mountain Trench along the eastern margin of British Columbia and southward into northern Montana. The northern reaches of the Trench were created by strike-slip faulting, whereas Eocene and younger normal faults configured the southern reaches of the Canadian Cordillera (Coney et al., 1980; Gabrielse, 1991; Grasby & Hutcheon, 2001). In the south-eastern area of British Columbia, the resulting valley trend separates folded and faulted early Palaeozoic strata to the east from igneous and metamorphic rocks of the Omenica Belt to the west. The regional Purcell Thrust trends NW-SE northward of Radium, then turns to the south-west at Radium (Figure 1). Numerous Quaternary travertine and tufa-forming springs aligned along the NW-SE oriented Cordilleran foreland in western Canada. In particular, tufa and tufa-travertine deposits aligned along the eastern side of the Rocky Mountain Trench in south-eastern British Columbia and eastward into the foothills of south-western Alberta (Figure 1). Eastward of the Purcell Thrust, most springs aligned between the extensional faults along the margin of the Rocky Mountain Trench and the Redwall Thrust, which merges with the Purcell Thrust at Radium.

The Wolfenden deposit is one of the post-glacial tufa accumulations aligned along the eastern margin of the Rocky Mountain Trench (Grasby & Hutcheon, 2001). It is located along the eastern side of the Purcell Thrust, northwest of the town of Radium. The area coincides with the eastern side of the Columbia River Valley and follows the Rocky Mountain Trench physiography in south-eastern British Columbia (Figure 1). A valley glacier occupied the length of the Trench until the end of the Pleistocene. Northward retrenchment probably resulted an ice-free valley approximately 10 000 years BP (Fulton, 1971; Rainey & Jones, 2010). The glacier retreat permitted the activities of vents for bicarbonate-laden springs along the valley margins. Tufa deposits accumulated on the bedrock of lower Palaeozoic carbonate strata and thinned glacial deposits.

These calcium carbonate depositional processes varied with the range of water temperatures and solute chemistry (Grasby & Hutcheon, 2001). They vary from thermal springs such as the famed Fairmont Hot Springs to cooler water deposits elsewhere, including the Wolfenden tufa. Stable isotope analyses ($\delta^{13}C$, $\delta^{18}O$) indicate that all of the thermal and cooler spring waters have meteoric origins and were heated to a wide range of temperatures responsive to groundwater circulation depths and impact by the geothermal gradient (Grasby et al., 2000). Deep circulations of meteoric water in the eastern Cordillera may have been as much as 2.5–5 km along faults associated with the Rocky Mountain Trench and other crustal fault

systems (Allen et al., 2006; Grasby et al., 2000; Grasby & Hutcheon, 2001). Temperatures have been recorded by Grasby et al. (2000) using various geothermometry guides at the surface (*T*meas °C) and indirect measurements for deep seated circulations (*T*max °C). Examples of (*T*meas °C; *T*max °C) are: Wolfenden (28°; 36°); Cave and Basin (30°–32°; 52°–59°); Miette (52°; 85°); Radium (44°; 69°); Fairmont (47°; 62°). Other direct temperature measurements for the Main Vent at the Fairmont Hot Springs have been recorded from 30 to 49°C (Rainey & Jones, 2009).

Thermal springs in this area of the south-eastern Canadian Cordillera developed chemical compositions that were kinetically in equilibrium with the host rocks (Grasby et al., 2000). Some thermal springs record activities of sulphate-reducing microbes with water chemistry including dissolved gypsum or other sulphur compounds. In contrast, many springs in the foothills of south-western Alberta do not precipitate calcium carbonate and do not result in tufa deposits (Borneuf, 1983). This difference relates to tufa depositing conditions to the west that were responsive to water chemistry consisting of magnesium-bicarbonate solutes, in contrast to water eastward into the foothills of western Alberta that contain calcium–magnesium-sulphate, sodium sulphate and sodium chloride. These differing chemical regimes are linked to the prevalence of thick sections of carbonate strata in eastern British Columbia compared to thin or absent carbonate strata eastward into Alberta.

3 | STUDY AREA

The Wolfenden tufa deposit has been quarried at a location approximately 1 km east of the village of Brisco in the mountainous East Kootenay area in south-eastern British Columbia (50°50′ lat, 116°16′ long.) (Figure 2). The site is between the Hot Springs tufa deposit to the northwest and the famed Fairmont Hot Springs deposit to the south-east (Figure 1). The quarry is located along the eastern floodplain margin of the Columbia River Valley at an elevation of 910 m a.s.l. at the base of an elevated mountainous ridge of dolomitic strata formed as the eastern margin of the Rocky Mountain Trench (Figure 1). The main exposure of the Wolfenden tufa is a now abandoned quarry site, which has been backfilled and mechanically covered over with the previously excavated tufa blocks and rubble (Figure 3A). The quarry wall is inaccessible.

The Wolfenden tufa is approximately 7 m thick with a 100–150 m wide apron extending westward, downslope, for at least 200 m. Other than the site of the quarry, the deposit apron is almost entirely covered by topsoil and dense vegetation. The quarry face, now backfilled, is adjacent to the source vent, a 15–20 m diameter pond located 100 m upslope to the east (Figure 2). The 100 m distance between the quarry face and the vent is covered by dense vegetation and topsoil, but weathered and dislodged blocks of tufa protrude at the surface. This ponded vent appears to be inactive and no runoff occurs at this site, but hydraulic pressure maintains the water level near the surface. Excess flow is routed in the subsurface and feeds the Wolfenden Creek a few hundred metres to the south (Figure 2). Wolfenden Creek is an active 1–1.5 m wide spring that flows westward toward the Columbia River. It terminates in a small water-saturated boggy sump, 10 m diameter, at an elevation of 815 m a.s.l. along the eastern bank of the Columbia River (Figure 2). This creek actively precipitates calcium carbonate on the floral debris and cobbles.

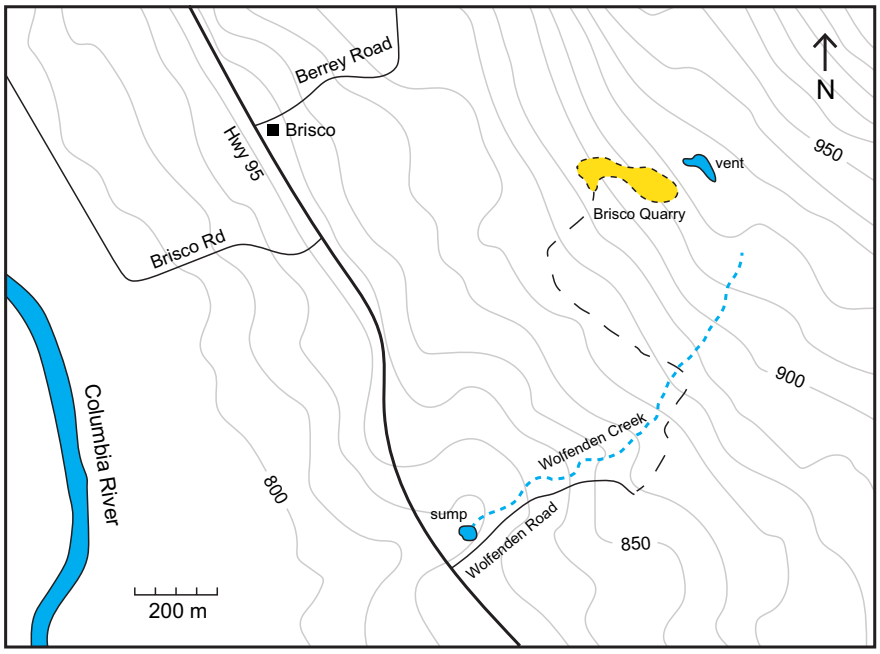

FIGURE 2 The location of the Brisco Quarry in south-eastern British Columbia. The Wolfenden tufa deposit and adjacent vent are along the eastern Columbia River valley at the base of mountainous terrain of the eastern Rocky Mountain trench. C.i. = 10 m a.s.l.

FIGURE 3 The Brisco Quarry and excavated blocks of the Wolfenden tufa stockpiled on the quarry floor. (A) Abandoned quarry face backfilled and covered over by tufa blocks and rubble. (B and C) Stockpiles of excavated but not shipped tufa blocks remain on the quarry floor, some with 6 cm diameter core holes.

The vent associated with the Wolfenden tufa deposit cuts dolomitic strata of the Beaverfoot Formation (U. Ord.-M. Silurian) along the eastern margin of the Columbia River Valley, which coincides with the eastern margin of the Rocky Mountain Trench (Evans, 1933). The carbonate strata overlie fine-grained clastic sediments of the McKay Group (Cambrian-Ord.), which floor the Quaternary deposits of the Columbia River Valley. The Wolfenden tufa deposit accumulated along the contact between McKay and Beaverfoot strata. Although partially obscured by surficial deposits, the tufa extends from the vent in the Beaverfoot Formation downslope onto bedrock consisting of dark red siltstones of the McKay Group. The thickness, if any, of the Quaternary sediment between the tufa and the Early Palaeozoic bedrock is not known.

The quarry at the Wolfenden tufa deposit is locally known as the Brisco Tufa Quarry or by the trade name of Rocky Mountain Tufa. The quarrying activities in the years from 1999 to 2002 sourced tufa rock for ornamental gardens and other landscaping projects. Shipments were 900 metric tonnes in 1999, 1000 tonnes in 2000, 1000 tonnes in 2001, and 2000 tonnes in 2002 to retail garden supply markets across Canada and the United States. Following these shipments, the quarry was abandoned. The 100 m long quarry face has been covered over with previously the excavated tufa blocks and rubble (Figure 3). Stockpiles on the quarry floor sourced specimens for this research. Direct access to the quarry face is impossible to ascertain tufa stratigraphy for sampled material.

Records of the British Columbia Department of Mines do not have any reference to stratigraphic information or reliable information on the coring operations that occurred at the site. The stratigraphic context of the research material is constrained by the lack of direct sampling across the now obscured quarry face. Nonetheless,

hundreds of tonnes of excavated tufa rock remain on the quarry floor (Figure 3B,C), having been excavated for commercial purposes but unshipped. Many of the tufa blocks in these stockpiles have been core drilled, resulting in 5–20 cm long and 4–6 cm diameter cored intervals that are also stockpiled on the quarry floor (Figure 3C). These detriments may have been instrumental as to why the Wolfenden deposit has been overlooked by most previous researchers on the origin of eastern Rocky Mountain tufa deposits.

4 | PREVIOUS WORK

The origin, age, facies and depositional environment of numerous tufa deposits in the eastern Rocky Mountains, western Canada, have been extensively documented by research projects of the Geology Department at the University of Alberta (Rainey, 2009; Rainey & Jones, 2007, 2009, 2010; Turner & Jones, 2005). Rainey (2009) provides the only reference, albeit cursory, regarding the Wolfenden tufa and records limited data on $\delta^{13}C$ and $\delta^{18}O$ stable isotopes. Otherwise, there are no published studies regarding the Wolfenden tufa. Previous field work by D. Rainey, University of Alberta, on lithofacies of the nearby Hot Creek tufa deposit included limited sampling at the Wolfenden site when the quarry operations were active. The stratigraphic context of these Wolfenden samples were not recorded. Research on the Wolfenden deposit was abandoned by the University of Alberta, excepting for some SEM images made available without commentary to the author. Some of these SEM images have been included with permission in this study. There are data available on the water chemistry of the nearby Wolfenden spring (Grasby et al., 2000; Grasby & Hutcheon, 2001).

5 | METHODOLOGY

5.1 | Sample collection

Tufa samples, approximately 50 kg, were collected during the 2021 field season from stockpiles of the previously excavated material at the now abandoned quarry. All samples collected were not in situ since the quarry face has been covered over with previously excavated blocks and rubble (Figure 3). Tufa stockpiles consisting of hundreds of tonnes of excavated blocks and cored tufa remain on the quarry floor. Partially buried tufa blocks exposed along the margins of the quarry and the downslope tufa apron were also deemed to have been dislodged.

More than 100 samples were collected. Of these, 25 were selected for thin-sections based on textural and lithofacies variations. All samples used for chemical analyses were crushed and powdered from sawn blocks of tufa used for making thin-sections. About 10 g was powdered using tungsten carbide grinding tools. Splits of 2 g each were submitted to chemistry laboratories for isotope and trace elements measurements.

5.2 | Petrography

Petrographic thin-sections were prepared from slab-sawed sections of tufa blocks and cored intervals at the Calgary Rock Services Laboratory. Portions of these sawn slabs were embedded in epoxy to facilitate the manufacture into 25 thin-sections. All thin-sections were stained with alizarin red.

5.3 | Powder X-ray diffraction

The X-ray diffraction (XRD) analyses of randomly selected sample utilised two diffractometer instruments: (1) Xpert Pro X-Ray Diffractometer with a copper radiation source and Rietveld refinement with settings at 40 mA, 45 kV, located at Calgary Rock Services laboratory; (2) Bruker D4 Endeavour XRD with a Lynx-Eye detector, using a cobalt radiation source and a nickel Kß filter with generator settings at 40 mA and 35 kV located at AGAT Laboratory, Calgary.

X-ray diffraction analysis of samples on the Xpert instrument confirmed calcite as the bulk mineralogy in contrast to aragonite. Multiple randomly selected samples were examined on the Bruker instrument for the presence of calcium carbonate polymorphs with instrumentation setting of half-step theta. Step size °2Θ was 0.01 with half-steps and step scan time of 5 s.

5.4 | Scanning electron microscopy

The scanning electron microscopy (SEM)-EDS instrumentation is a FEI QEMSCAN 650 and an Amray 1820 upgraded with a 4 pi Digital Control and Image Acquisition System, operated with 30 kV voltage and 45 uA current, located at the Calgary Rock Services laboratory. Samples were sputtered with particulate gold. The X-ray fluorescence and X-ray fluorescence elemental analyser instrumentation were an Orbis PC Micro-EDXRF Elemental Analyser XRF with Rh as an X-ray source. Supplemental SEM imaging of specimens collected by D. Rainey used a JEOL 6301F field emission instrument at an accelerating voltage of 5–10 kV, located at the University of Alberta, Edmonton.

5.5 | Stable isotopes

Measurements of $\delta^{13}C$ and $\delta^{18}O$ were obtained by the continuous flow isotope ratio mass spectrometry (CF-IRMS) methodology using a Thermo Finnigan (Thermo Fisher) Gas Bench coupled to a DeltaV-Plus instrument at the Department of Geoscience, University of Calgary. Each sample was crushed, ground and sieved to a powder of 50–100 μm particle size. Each powdered sample containing approximately 0.3 mg of calcite was placed into a vial and injected with approximately 200 μl of anhydrous phosphoric acid, using the methodology described by Coplen et al. (1983). Each sample vial was capped and flushed with helium for 10 min at a flow rate of approximately 70 ml/min. The vial was subsequently rotated to ensure sample reaction. Samples were then placed in the heated block of the Gas Bench at 25°C for 5 h. The resulting carbon dioxide emissions were analysed using a Gas Bench using a 50 μl sample loop sourced to the mass spectrometer. The gas sample in each vial was measured six times by loop injection. The first measurement was routinely rejected and the five subsequent measurements recorded. Stable isotopes are measured as mille (‰) values, noted as parts per thousand difference between the isotope ratios of the samples and that of the standard (Vienna-Pee Dee Belemnite; VPDB). Oxygen values are reported relative to VPDB. Precision of this methodology is better than ±0.1 ‰ for both $\delta^{18}O$ and $\delta^{13}C$.

5.6 | Charcoal ^{14}C dates with accelerator Mass spectrometry

The radiocarbon date of a single charcoal-rich sample from the Wolfenden tufa (Figure 4) was determined by accelerator mass spectrometry (AMS) at the Lalonde AMS Laboratory (Kieser et al., 2015), University of Ottawa, Ontario, using procedures documented by Crann et al. (2017). This specimen was the only charcoal-bearing sample observed at the tufa deposit. Pre-treatment of the bryophyte charcoal material underwent a standard acid-alkali-acid bath described by Brock et al. (2010). Any CO_2 absorbed during the alkali step was removed with a second HCl acid wash, then freeze-dried. The sample was combusted using a Thermo Flash 1112 elemental analyser in CN mode, interfaced to trap pure CO_2 in a prebaked Pyrex breakseal. The weight of the solid organic material was recorded before it was placed into a tin capsule for combustion and graphitisation. The recorded sample of pure CO_2 in a 6 mm breakseal was converted to elemental carbon following the procedure of St-Jean et al. (2017), a process that takes 2–3 h to complete. The graphitised sample was pressed into a target form using a pneumatic press. Analysis of ^{14} C was recorded on a 3MV tandem accelerator mass spectrometer. Ions of $^{12,13,14}C^{+3}$ were measured at 2.5 MV terminal voltage on the instrument. The fraction of modern carbon ($F^{14}C$) was calculated using the methodology described by Reimer et al. (2004) with the sample $^{14}C/^{12}C$ ratio compared to a standard. The ^{14}C age is calculated as −8033In ($F^{14}C$) and reported in ^{14}C years BP (benchmarked as AD 1950), using the techniques documented by Stuiver and Polach (1977). The calibration curves use OxCal 4.4 software (Bronk Ramsey, 2009) and the IntCal20 Northern Hemisphere Radiocarbon Calibration Curve (Reimer et al., 2020) with material codes of Crann et al. (2017).

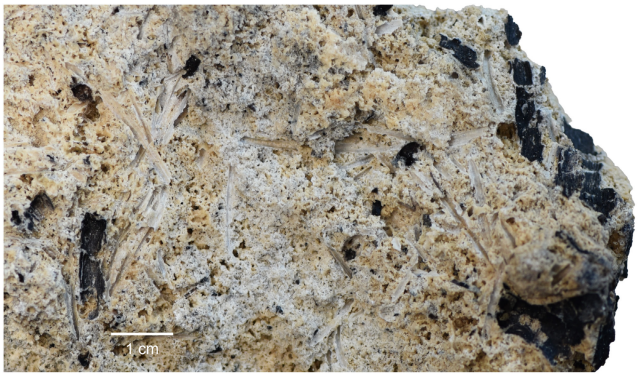

FIGURE 4 Bryophyte pith charcoal disseminated in a block of tufa dislodged from the quarry wall 1 m below the top of the deposit. The ^{14}C date records 2200 years BP.

5.7 | Inductively coupled plasma mass spectrometry

Three samples were analysed for the presence of trace elements using a sodium peroxide fusion-mass spectrometer (ICP-OES/ICP-MS) at the AGAT Laboratory, Toronto. The finely ground samples were fused with sodium peroxide and sodium hydroxide in a muffle furnace for 30 min. The resulting cake was dissolved in nitric acid and completed to 100 ml with de-ionised water. Perkin Elmer 7300DV/8300DV ICP-OES and Perkin Elmer ELAN 9000/NexION ICP-MS instruments were used with inter-element correction techniques to correct for spectral interferences.

The samples were analysed as percentages or ppm units for: Ag, Al, As, B, Ba, Be, Bi, Ca, Cd, Ce, Co, Cr, Cs, Cu, Dy, Er, Eu, Fe, Ga, Gd, Ge, Hf, Ho, In, K, La, Li, Lu, Mg, Mn, Mo, Nb, Nd, Ni, P, Pr, Rb, S, Sb, Sc, Si, Sm, Sn, Sr, Ta, Tb, Th, Ti, Tl, Tm, U, V, W, Y, Yb, Zn and Zr.

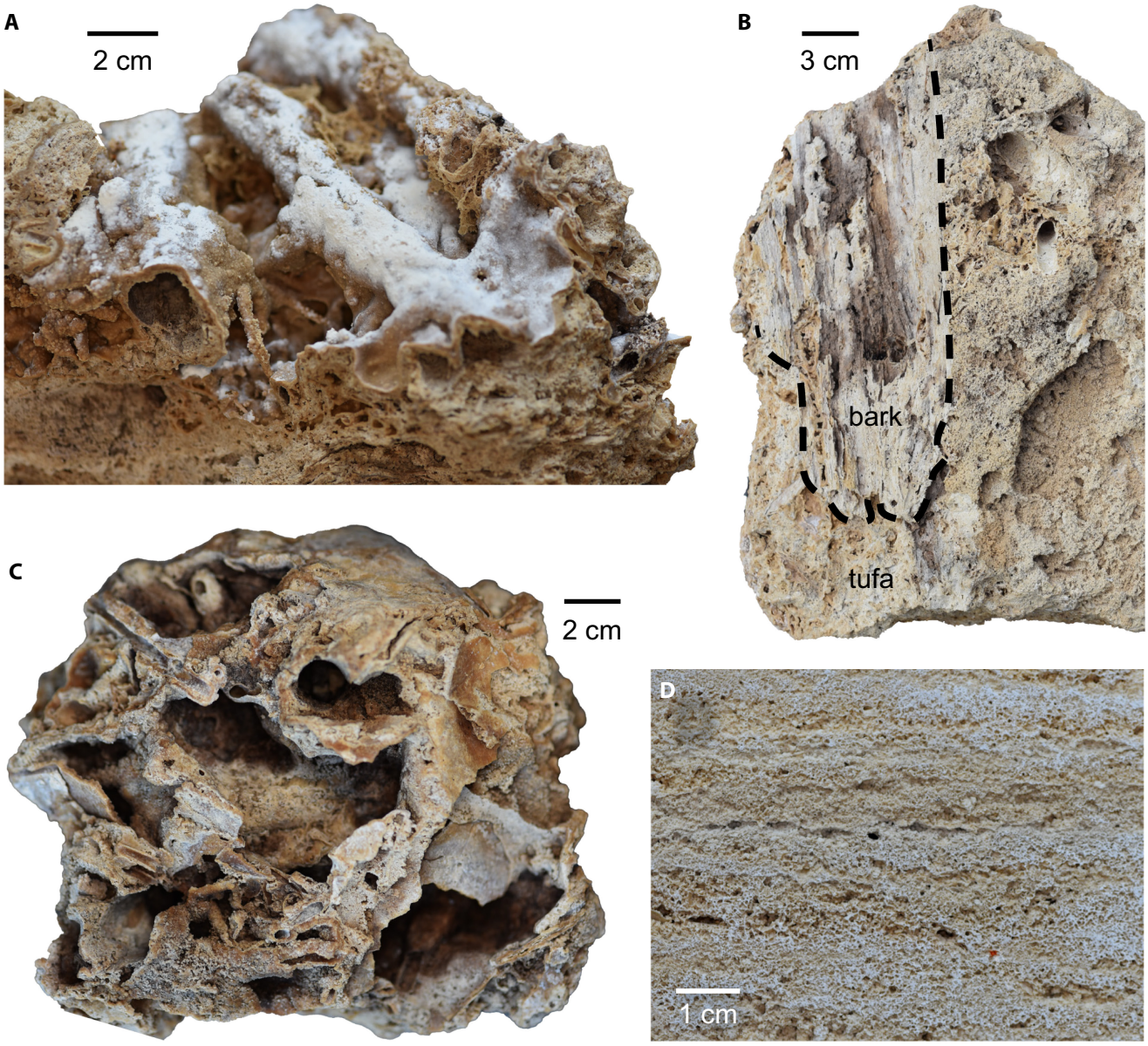

FIGURE 5 Textures of the Wolfenden tufa. (A) Extensive mouldic porosity developed from encrustation of plant debris, subsequently decayed. Larger mouldic porosity areas often include calcite encrusted algal filaments. (B) Calcified tree bark fragment embedded within the tufa. (C) Cavernous mouldic porosity resulting from decay of floral debris. (D) Tufa from the thinned downslope edge of the deposit consists of cm-thick beds characterised by parallel laminae with mm-scale bubble mouldic porosity and calcified algal filaments.

6 | RESULTS AND INTERPRETATIONS

6.1 | Stratigraphic context

The 7 m thick tufa deposit has a variable mixture of morphotypes from flat horizontal beds to curvilinear and hummocky beds. The stratigraphic contexts are not discernable. Bryophyte facies are abundant but it was impossible to determine the overall lateral and vertical extent. The quarry face has been covered over and observations of any relevant bedding details larger than a metre scale were not possible. Although overall stratigraphic organisation is indeterminate, bed characteristics at intervals tens of centimetres thick are recognisable on many of the larger displaced blocks of tufa.

All tufa blocks derived from the quarry face incorporate varying concentrations of calcite encrusted bryophyte flora, algae and cyanobacteria (Figures 5 through 8). This bryophyte-dominant tufa deposit has bedding textures discernable by the orientation and cluster arrangements of the tubular mouldic porosities (Figure 7). Most tufa specimens, tens of centimetres across, display tubules of bryophytes with unidirectional orientation representative of vertical growth positioning, in contrast with more fragmented tubules accumulated along the sub-horizontal depositional surfaces representative

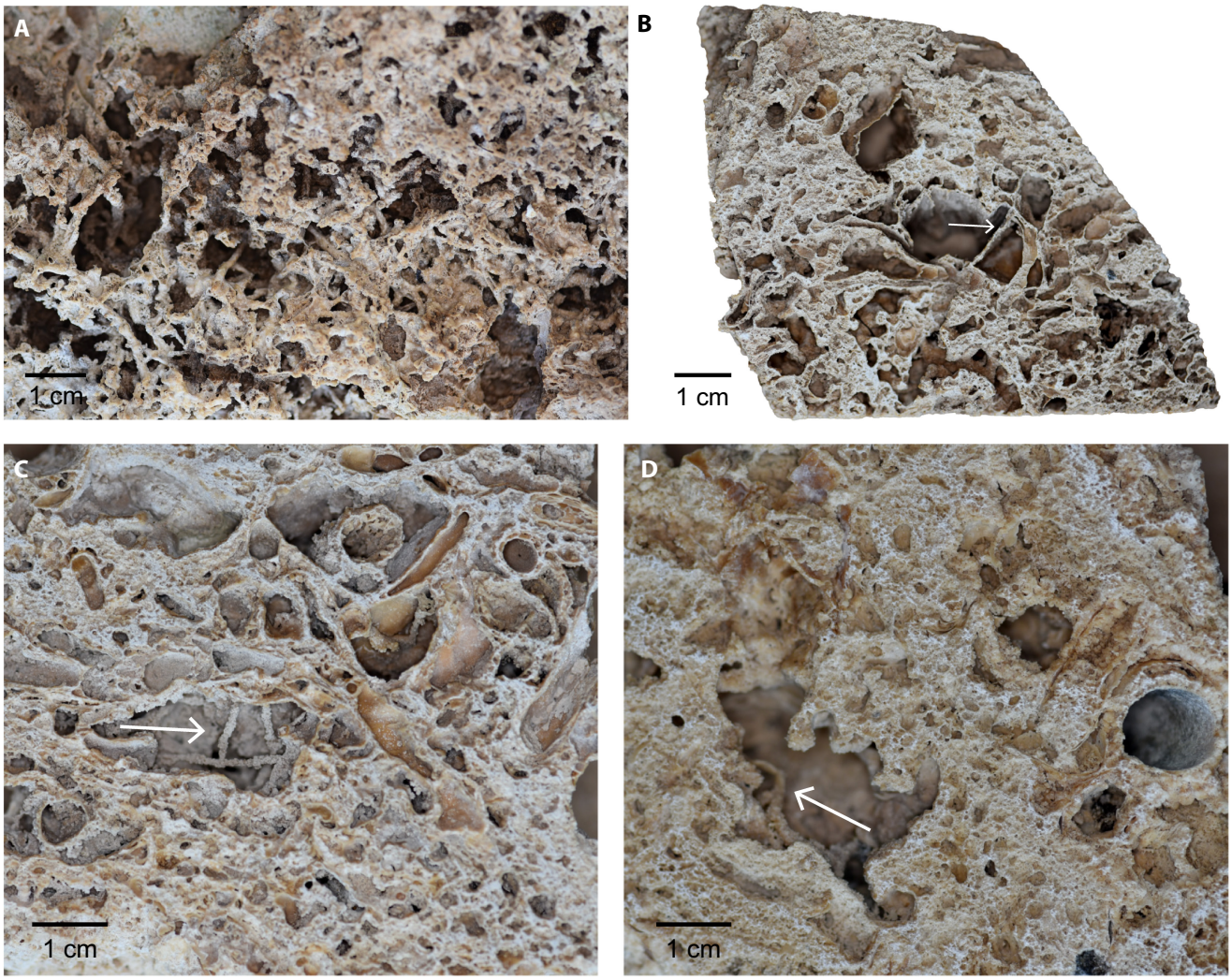

FIGURE 6 Mouldic porosity characterised by calcite encrusted algae. (A) Large multi-chambered porosity complex with interior meshwork of calcite encrusted algae. (B–D) Mouldic porosity areas, 1–2 cm across, commonly contain calcite encrusted algal filaments extending between walls (arrows).

of shallow burial. About 10% of the specimens display two divergent orientation sets consistent with bryophyte hummocks, often with a 2–3 cm-thick zone of calcite shrub fabrics emplaced between the two orientation sets. Larger, 10–20 cm or more, calcified fragments of bark of twigs and tree branches of uncertain floral taxonomy have been preserved within the tufa (Figure 5B). These several millimetre to centimetre-thick bark fragments preserve smoothly textured surfaces suggestive of the modern aspen or birch. Curvatures of some larger specimens suggest fragmentation of trees as much as 20–25 cm in diameter. The tufa deposit does not appear to preserve any tree stumps or subsurface rooted remnants.

The thinned (*ca* 1 m thick) tufa apron, extending 150–200 m downslope from the quarry face, is characterised by a finer grained texture consisting of centimetre-thick horizontal bedding (Figure 5D). These distal deposits lack any discernable evidence of bryophyte debris.

6.2 | Mineralogy and trace elements

The XRD analyses of five randomly selected samples indicate a consistent bulk mineralogy throughout the deposit, consisting of calcite (99.3%–99.9%), quartz (0.2%–0.4%), MHC (*ca* 0.2%–0.4%), and lesser amounts of anhydrite, portlandite and dolomite (protodolomite) (<0.1%). The trace presence of portlandite in all samples would be the result of the transformation of ACC to MHC (Swainson, 2008). The XRD analyses do not record the presence of non-crystalline ACC. In contrast, this calcium carbonate polymorph can be differentiated by SEM imaging.

Three tufa samples were analysed for 58 trace elements. These results were mostly recorded as near or below detection limits (DL). In contrast, Table 1 records 10 elements of the analyses that are relevant, either by their notable concentration or lack thereof.

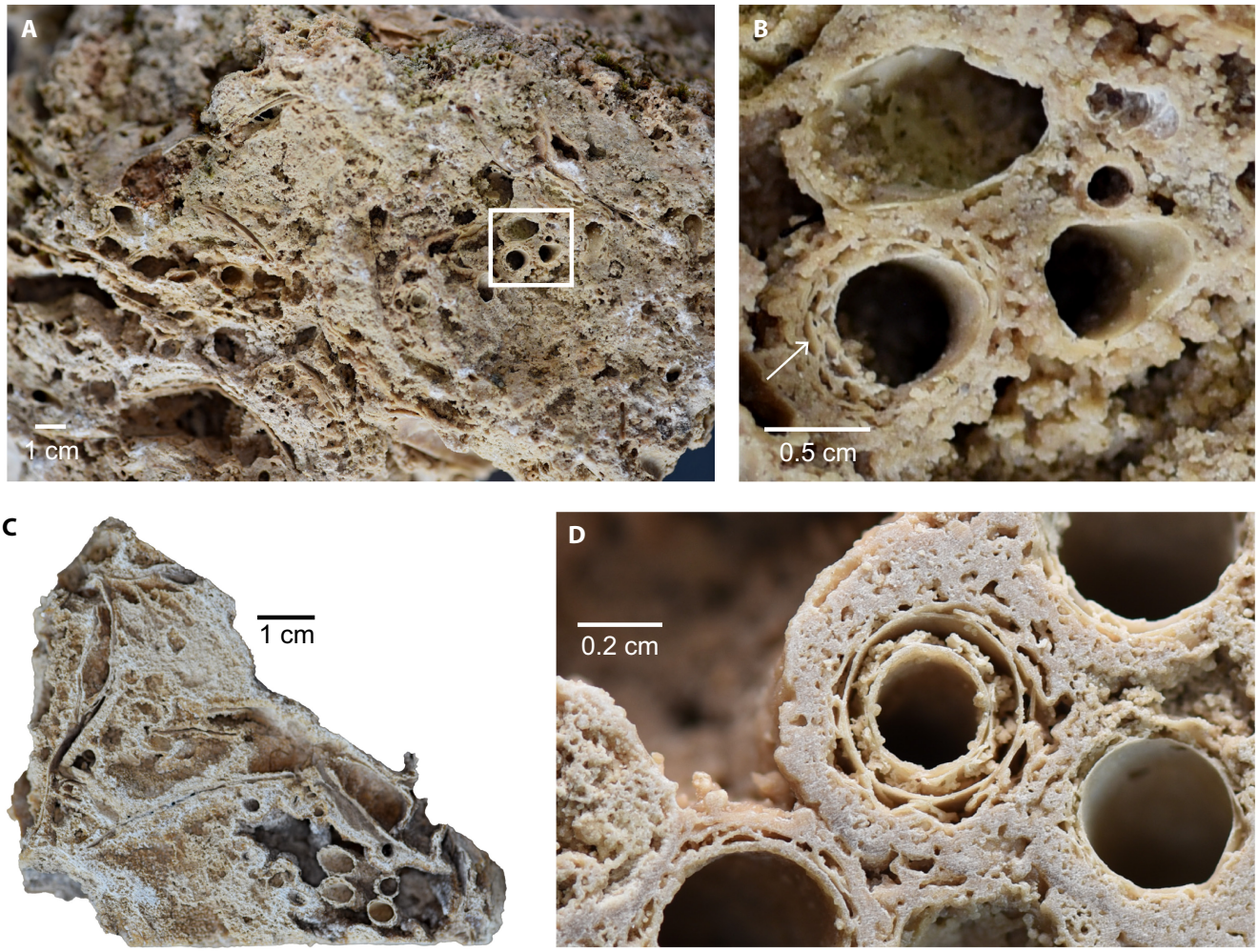

FIGURE 7 Tubular mouldic porosity resulted from calcite encrusted bryophytes, a dominant fabric of the Wolfenden tufa. (A) Typical example of a cluster of multi-centimetre long bryophyte tubules. (B) Enlarged area of a (frame) detailing the encrustation fabric consisting of concentric growth layers with aggregates of mesocrystalline calcite (arrow) bridging the concentric growth layers. (C) Encrusted bryophyte tubules are often preserved within larger mouldic porosity chambers, resulting from decay of densely packed floral debris encasing the bryophytes. (D) Meshwork of calcified algae extend outward from concentric growth layers encrusting bryophyte stems. The calcite encrustation fabric results from precursor amorphous calcium carbonate transformation to monohydrocalcite and subsequently to calcite.

The relatively high concentrations of Mg, Sr and Ba indicate the adsorption of these metal ions into the calcium carbonate crystallographic structure. These elements widely occur in marine depositional environments that include limestone and dolomite strata. Magnesium is also common to clay, but the level of clay in the Wolfenden tufa is markedly low. The lack of a significant concentration of Al and Si indicates that the groundwater sourcing the tufa deposit transported minimal silt of quartz and clay. The source of these elements in the Wolfenden tufa is attributed to calcium-rich groundwater that has permeated the dolomitic strata of the adjacent bedrock. The high levels of Mn, S, U and Zn are commonly associated with organic debris.

6.3 | Encrusted organic debris and mouldic porosity

The distribution of densely packed bryophyte plants resulted in a pervasive tubular mouldic porosity fabric, characterised by encrustations consisting of multiple concentric growth layers of calcium carbonate (Figure 7). These fossilised bryophyte stems consist of 1–10 cm or longer tubule lengths with 4–10 mm diameters. These mouldic porosity tubules cluster in vertical and sub-horizontal positions. Most specimens (60–80%) have been preserved as moderately sinuous, curvilinear lengths in sub-horizontal positions, representative of shallowly buried accumulation with modest burial deformation indicative of pre-decay pliability responsive to water saturation. The encrusted tubules are

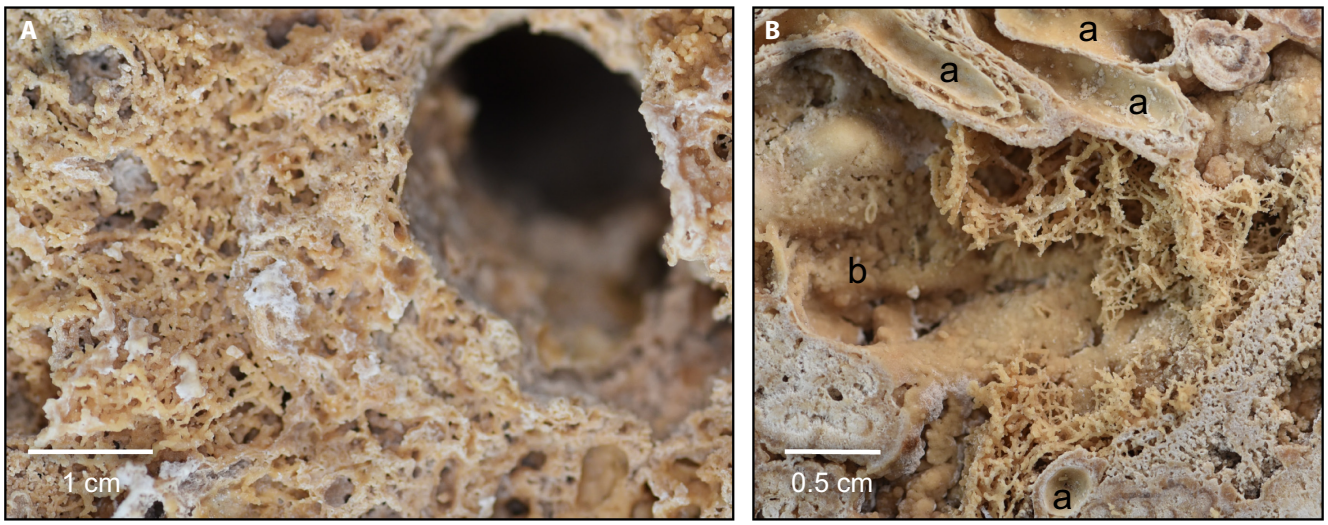

FIGURE 8 Wolfenden tufa fabrics mostly consist of a loose meshwork of calcite encrusted algae enveloping cm-diameter mouldic porosity chambers resulting from decay of bryophytes and packed floral debris. (A) Multi-cm thick meshwork of calcite-encrusted algae envelope cm-diameter mouldic porosity chamber. (B) A lattice-like meshwork of calcified algae partially infill mouldic porosity between encrusted bryophyte tubule fragments (a) and partially mouldic porosity (b).

TABLE 1 Trace elements of three tufa samples

Element	Al (%)	Ca (%)	Ba (ppm)	Mg (%)	Mn (ppm)	S (%)	Si (%)	Sr (ppm)	U (ppm)	Zn (ppm)
DL	0.01	0.05	0.5	0.01	12	0.01	0.01	0.01	0.05	5.0
No. 1	<0.01	39.8	35.4	0.35	<10	0.88	<0.01	978	1.23	33
No. 2	0.04	38.8	38.8	0.33	38	0.83	0.09	894	1.24	40
No. 3	0.03	39.8	39.0	0.34	12	0.86	0.04	1030	1.18	10

sometimes split-open lengthwise due to burial compaction (Figure 8B). Most interiors of these tubules, now mouldic porosity resulting from decayed pith, have not been occluded by cement. Interiors of carbonised pith are rarely preserved (Figure 4), but useful for ^{14}C age dating.

Voluminous mouldic porosities have also resulted from the encrustation of wads of organic debris such as matted leaves that subsequently decayed. Many specimens display multi-centimetre long contorted cavities as much as 5–10 cm long and 4–5 cm wide (Figures 5A,C, 6 and 8). Larger mouldic porosity chambers (>1 cm) have been bridged by calcite encrusted algae. Encrusted filaments, 1–2 cm long and 1–2 mm thick, are distributed as lattice-like meshwork and as individual structures that bridge opposite cavity walls. These filaments are encrusted by micro-bulbous crystalline aggregates.

Many of the bryophyte encrustation fabrics consist of inner and outer concentric growth surfaces, separated by 0.5–1 mm (Figure 7B,D). Microcrystalline aggregates of calcite bridge these tubular structures and provide structural stability. Other tubular specimens are thicker, resulting from coalesced outer and inner tubules. The outer concentric growth surface tubule would have resulted in calcium carbonate precipitation on the epidermis of the bryophyte stem. The interior of each of these concentric growths is usually covered by a thin laminar layer of calcium carbonate with a mesh-like honeycomb texture (Figure 7B-arrow, or partially encrusted by patchy distribution of crystalline aggregates (Figure 7B,D). Calcite precipitation within irregular shaped and tubular form mouldic porosities consist of an open meshwork of calcite-entrusted algae (Figures 6A and 8). This lattice-like meshwork of calcified algae may extend outward for 1–2 cm from the mouldic porosity sites. Widely dispersed smaller mouldic and bubble porosities also have open voids that are often partially infilled by encrusted 4–10 mm long algal filaments.

6.4 | Petrographic textures

6.4.1 | Micro-spheroids

The pervasive distribution of peloid-like micro-spheroids of micrite with diameters of 30–60 μm incorporate calcified EPS filaments (Figure 9). These innumerable

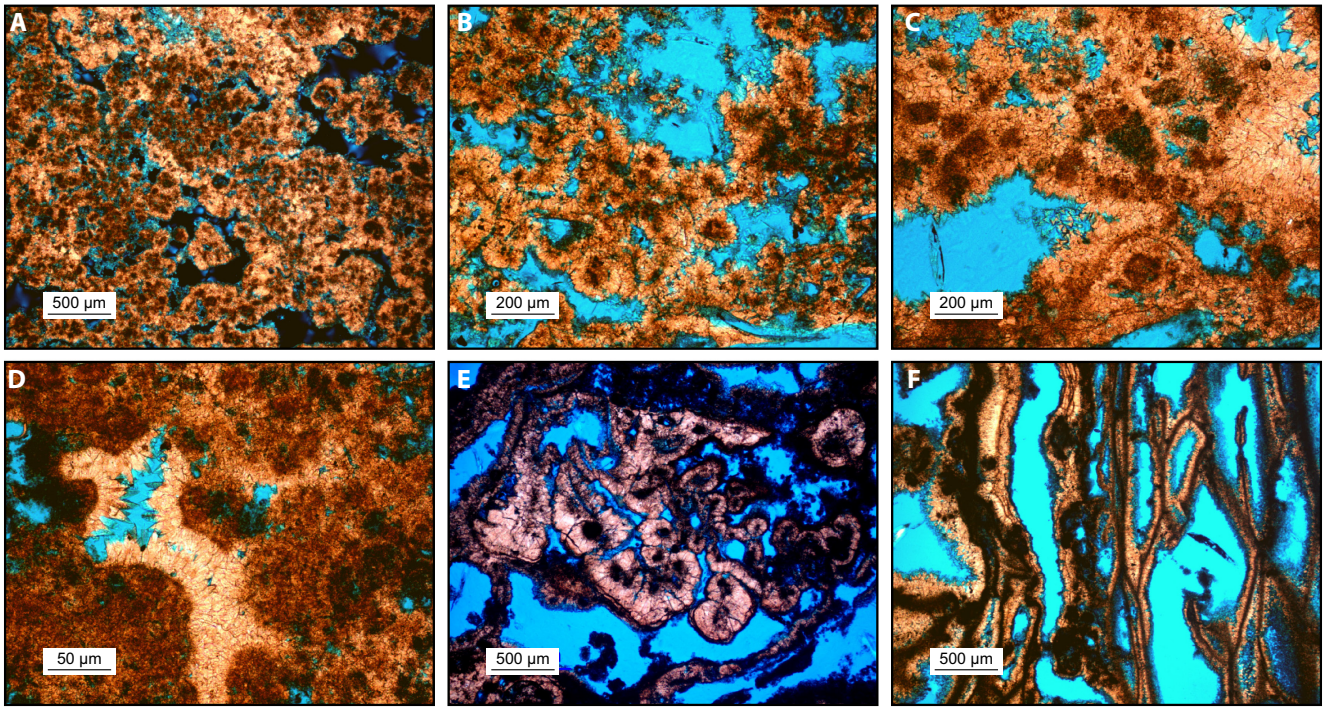

FIGURE 9 Pervasive distribution of peloid-like micro-spheroids of micrite with radial spar coronas. (A–C) Densely packed clusters of micrite spheroids infilling mouldic porosity with coronas of radial spar. (D) Detailed image of contact between adjacent spheroids with interlocked radial spar coronas. (E, F) Micro-spheroids often aligned along the inner surfaces of the mouldic porosity. This fabric fill is a definitive characteristic of the Wolfenden tufa. Photomicrographs with plane-polarised light.

micro-spheroids are readily discernable by their dark brown colouration. These micrite spheroids are widely distributed as individual entities or welded spheroids clustered within the mouldic porosity (Figure 9). These spheroids often display outermost growth surfaces consisting of radial micro-spar coronas. The micrite micro-spheroids are growth centres from which larger, 50–100+ µm long spar, and composite crystal domains grow outward into the available mouldic porosity. This clotted peloid-like fabric is a defining characteristic of the Wolfenden tufa.

Interpretation. These are microbial EPS-mediated spheroidal aggregates of micrite, often with coronas of radial-CC spar. The spheroids are similar to carbonate peloids commonly observed in lacustrine and other sedimentary deposits (Della Porta, 2015), but are not commonplace in most tufa deposits. They are similar to micrite peloids that result from the degradation of pre-existing calcite (non-marine) or aragonite bioclasts (marine). However, these peloid-like spheroidal aggregates of micrite observed in the Wolfenden tufa were not derived from degradation of the preexisting calcite such as the growth layers lining mouldic porosity.

The morphogenesis of these micrite spheroids is interpreted as ACC nucleation on EPS filaments distributed throughout the available mouldic porosity, followed by transformation to MHC and subsequently to micrite. Recrystallisation resulted in coronas of radial spar and interiors of micro-spar or mixtures of micrite and microspar with partial preservation of the calcified EPS filaments. Notably, these micrite spheroids do not cluster around aggregates of clay, unlike the nucleation sites commonly observed in lacustrine deposits (Claes et al., 2021).

6.5 | Nanoscale and micron-scale fabrics

Ultrastructure fabrics include nanoparticles and nanospheroids of ACC, nanocrystalline and mesocrystalline MHC, needle calcite and calcified EPS filaments. These nanoscale and micron-scale fabric components are associated with biofilm EPS matrix filaments and precipitation of calcium carbonate polymorphs encrusting algae, cyanobacteria, and bryophyte sheaths.

6.5.1 | Meshwork of EPS filaments

Microbial sheaths and other organic entities such as bryophyte surfaces are covered with densely packed distributions of ultra-thin linear calcified EPS filaments. The lengths of these filaments are highly variable, <100 to 500 nm, but less than 1.2 µm (Figure 10). Fabrics of these densely packed nanoscale EPS filaments are the defining characteristic of the Wolfenden tufa. These filaments are distributed as overlapped linear to slightly curvilinear rod-shaped forms with

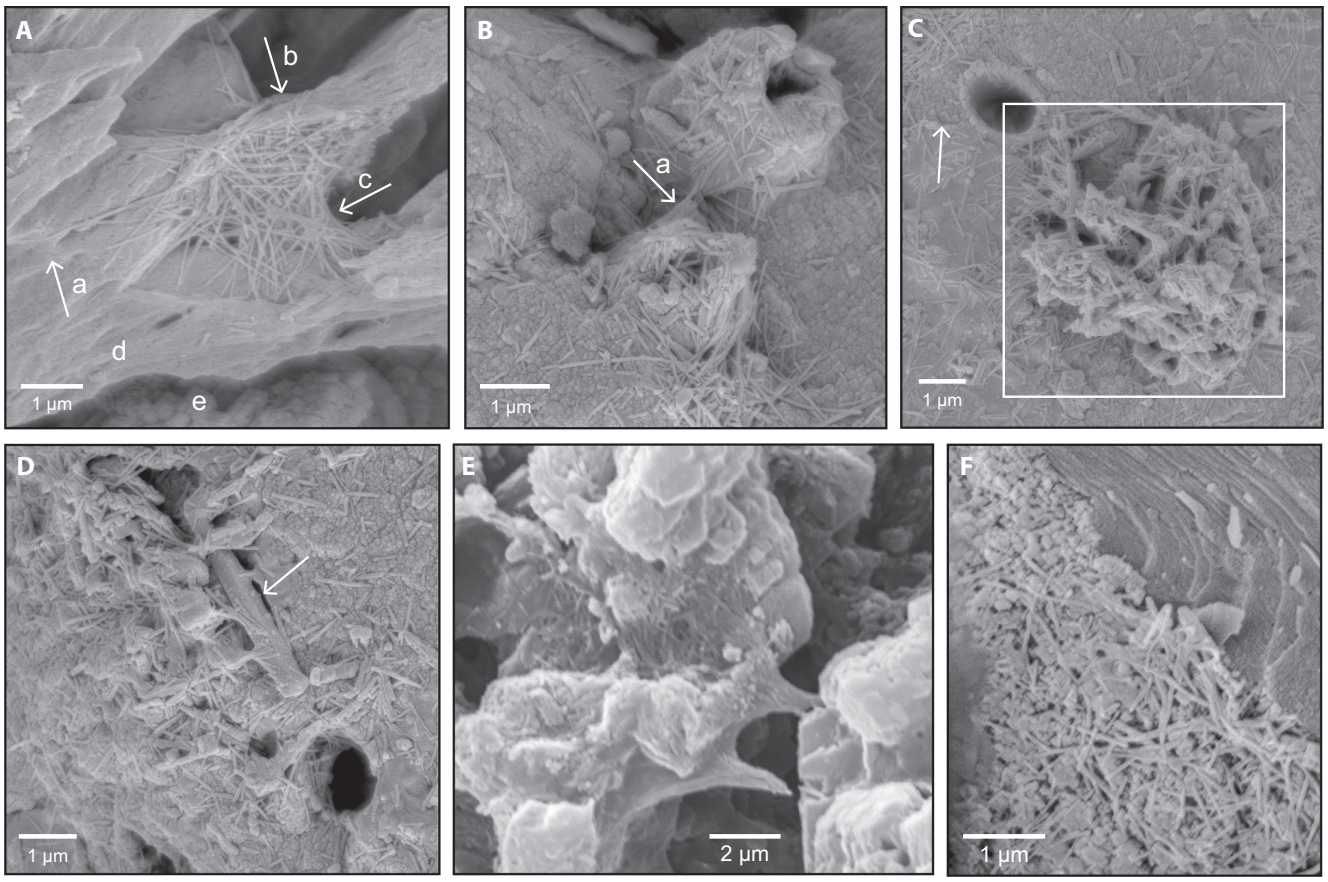

FIGURE 10 SEM imaging of the pervasive distributions of microbial-mediated linear EPS nanoscale filaments replaced by nucleation of calcium carbonate. Substrates of concentric growth layers of amorphous calcium carbonate nanospheroids were partially transformed to monohydrocalcite and calcite. (A) Concentric calcium carbonate growth surfaces on algae covered with netlike biofilm (b) covering clusters of nanoscale EPS filaments (c) anchored to substrates of calcite (a, d) and amorphous calcium carbonate (e). (B) Clusters of linear nanoscale EPS filaments and biofilm netting (a) on a cyanobacterial encrustation surface of partially coalesced nanospheroids of amorphous calcium carbonate. (C) Meshwork of fibrous EPS filaments (frame) attached by filamentous netlike biofilm EPS on substrate of densely packed nanospheroids of amorphous calcium carbonate (arrow). (D) Meshwork of calcified EPS filaments partially covering a calcified bacterium attached to substrate of amorphous calcium carbonate nanospheroids. (E) Mixture of monohydrocalcite and calcite nanocrystals with attachments of filamentous EPS to a substrate calcified EPS filaments, partially enveloped by layer of coalesced micrite. (F) Meshwork of calcified EPS nanoscale filaments, amorphous calcium carbonate nanospheroids, and mesocrystalline monohydrocalcite on the surface of a calcite crystal termination protruding into mouldic porosity.

variable nanoscale lengths contrasting with the thin but uniform diameter of *ca* 0.02 μm. All of these rod-shaped filaments have this consistent diameter. These nanoscale EPS rods, now calcified, are distributed as individuals but more commonly as clusters with amorphous netlike biofilms attached to each other and to the substrate (Figure 10).

Interpretation: The linearity of these rod-like forms and their wide range of nanoscale lengths are consistent with EPS filaments, which are biosynthesised extracellular polymeric substances that envelop microbes. The EPS, which consists of proteins, polysaccharides and DNA, often occurs as filamentous components of biofilms (Della Porta et al., 2022; Dupraz et al., 2004, 2009; Perri et al., 2021). The morphometric is too narrow to represent a fossil microbe. The clusters are often covered over by a biofilm netlike canopy (Figure 10A). Filamentous biofilms anchored by only a few cells can result in floating clusters of EPS filaments and microbes, now calcified (Janissen et al., 2015). These linear filaments often have ACC spheroids attached. Clusters of these EPS filaments are usually attached to a substrate consisting of arrays of partially coalesced ACC spheroids. These EPS filaments provided nucleation sites for ACC precipitates, resulting in their calcification. These EPS filaments are comparable to the nanoscale fibres described by Perri et al. (2012) as mesocrystals, and thereby represent calcified EPS filaments formed by low-Mg calcification of microbial films.

6.5.2 | Needle calcite crystals

The Wolfenden tufa is characterised by the widespread distribution of needle (needle-fibre) calcite crystals

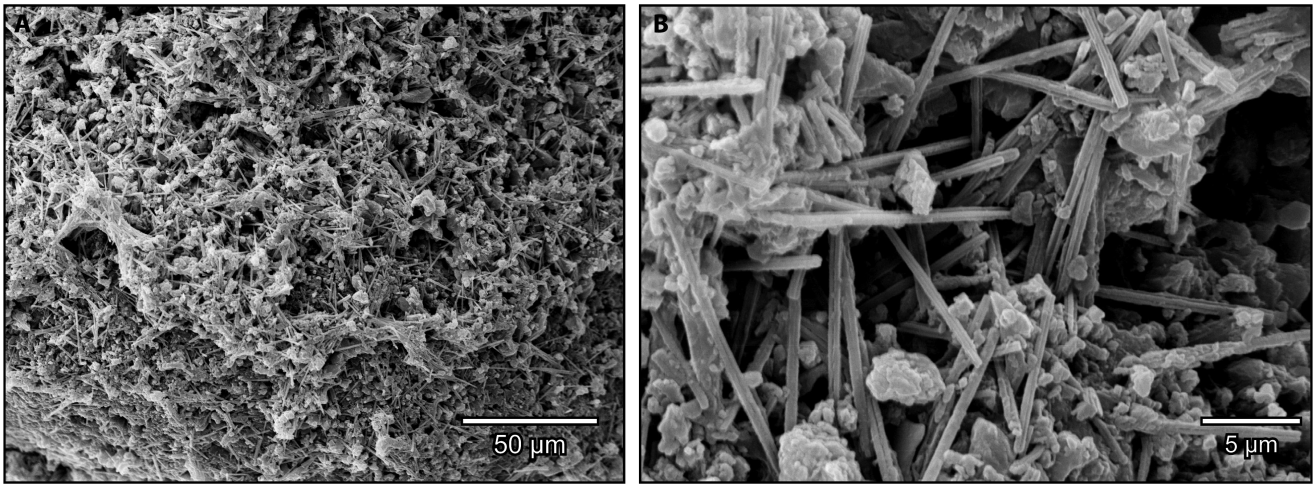

FIGURE 11 Distribution of needle crystals of calcite. (A) Clusters of 5–10 µ long calcite needles commonly develops within netlike biofilm canopies. (B) Each needle crystal is characterised by longitudinal groove. Morphogenesis of needle calcite, a definitive characteristic of the Wolfenden tufa, resulted from adsorption of Mg into the biofilm EPS-mediated amorphous calcium carbonate precipitate.

(Figure 11). These micron-scale crystals have 8–12 µm lengths and usually have serrated edges. Each of these needle crystals has a crystal habit characterised by a length-long longitudinal groove (Verrecchia & Verrecchia, 1994). These needle crystals are differentiated from calcified linear EPS filaments by their larger size (*ca* 10 µm vs <1 µm) and from calcified bacteria by the characteristic longitudinal groove. The needle crystals occur as scattered individuals and clustered as dense meshwork of randomly oriented crystals protruding outward from the substrate. These crystals are often loosely attached to the substrate, but also partially covered over and coalesced with larger platelets of calcite.

Extensive clusters of these needle crystals occur along areas hundreds of microns in length. These clusters are usually covered by a netlike biofilm canopy attached to the substrate or each other by fragments of an amorphous biofilm or filamentous EPS (Figure 11A). The pervasive distribution of these needle crystal fabrics with biofilm canopies is another defining characteristic of the Wolfenden tufa. Needle calcite crystals are known in other tufa deposits, but to the knowledge of this author, no other tufa has a comparable concentration.

Interpretation: Clusters of needle calcite crystals are interpreted to have developed within netlike biofilm canopies, followed by collapse and partial obliteration of the overlying biofilm (Figure 11A). This enveloping biofilm indicates that the crystal morphogenesis was a microbial process, but not the ACC-MHC-CC transformational process. There is abundant evidence, consisting of the biofilm association, that an EPS-mediated nucleation process was involved. In contrast, there is no direct evidence that the needle crystal formation included a precursor MHC polymorph transformation. A precursor ACC nucleation resulted in an ACC-CC transformation without the MCH as transitional polymorph stage. This is interpreted to have resulted from the adsorption of Mg into the calcium carbonate (ACC) precipitate within the biofilm with the result of a direct ACC-CC transformation. The morphogenesis of this needle crystal habit is consistent with elevated concentrations of magnesium and strontium reported by the trace element analyses. The magnesium in the spring water associated with the vent adjacent to the tufa deposit would have been sourced from dissolution of the dolomite strata.

The morphology of individual needle crystals and distribution of crystal clusters are consistent with the mineralogy and micron-scale crystal habits of moonmilk deposits, which characteristically include needle calcite and MHC (Borsato et al., 2000; Cailleau et al., 2009). Moonmilk is a mixture of calcium and magnesium carbonate minerals, mostly represented by calcite and MHC, but also magnesite, nesquehonite, huntite, and often gypsum and aragonite. Needle calcite is the dominant polymorph and crystal habit of moonmilk. The biotic or abiotic genesis of needle calcite in moonmilk is debated and remains unresolved (Borsato et al., 2000; Cailleau et al., 2009). Morphogenesis of needle calcite on cave walls without a moonmilk association is often interpreted as an abiotic depositional process responsive to rapid evaporation of supersaturated water (Jones & Peng, 2014). In contrast, the needle crystals of the Wolfenden tufa have a definitive biotic-EPS association.

The extensive distribution of micron-scale needle calcite crystals in the Wolfenden tufa have a superficial resemblance to moonmilk mineralogy. However, these needle crystal deposits of the Wolfenden tufa do not have the definitive texture of moonmilk consisting of a

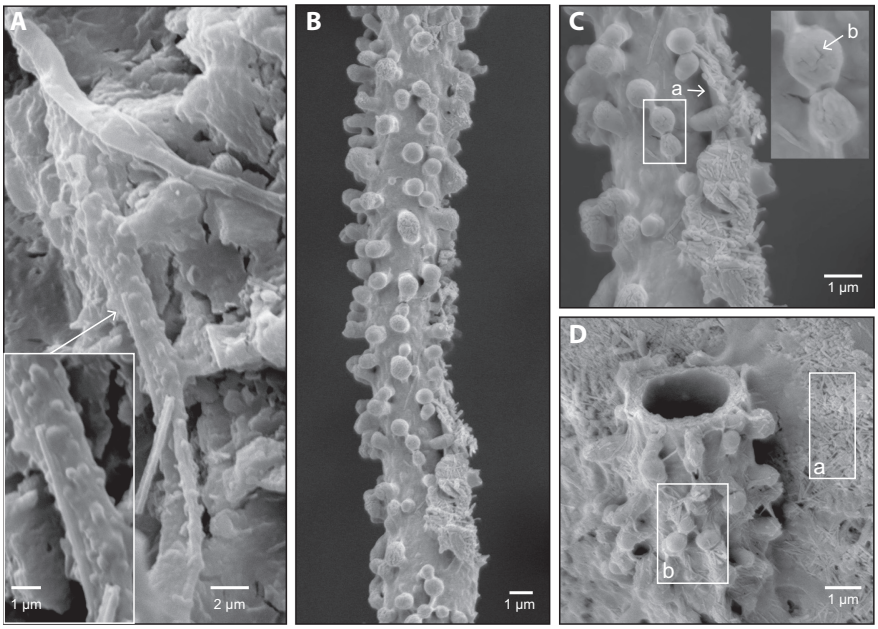

FIGURE 12 Cyanobacteria sheaths, 100 µm long and 1–2 µm diameter, with protuberances of ACC-MHC-calcite transformations. (A) Microbial filament with surface covered with nanoscale protuberances and formation of needle calcite crystals (frame) on the surface, and adjacent collapse-flattened calcified sheath. (B) Encrusted microbial filament covered with nanoscale fibrous EPS. Emergent concentric growth surface configured by 0.5 µm bulbous protuberances of amorphous calcium carbonate (ACC) and monohydrocalcite (MHC). These partially dislodge portions of previously formed crust. Innumerable calcified EPS nanoscale filaments are enveloped within the ultra-thin precipitations of ACC, resulting in concentric growth layers with extended protuberances. (C) Mesocrystalline MHC structures within the EPS-mediated ACC concentric growth layers and protuberances dislodge (arrow-a) earlier growth surfaces. Progressive dehydration of the ACC-MHC transformation results in development of nanoscale rhombohedral crystal faces of calcite (frame, arrow-b). (D) EPS filaments provide nucleation sites for the ACC precipitation and transformation to MHC, eventually resulting in calcification (frame-a) of the EPS filaments (frame-a) and protuberances (frame-b).

milk-like white powder or the moister plastic textured variety commonly deposited on walls of caves and ancient tombs. Nonetheless, the multi-centimetre long cavernous mouldic porosity (Figure 5C) would have created micro-environmental conditions with water/air-filled chambers having humidity comparable to conditions in caves, tombs and other types of sites with walls covered with moonmilk.

6.5.3 | ACC precipitation and ACC-MHC-CC transformations

Fabrics of the Wolfenden tufa consist mostly of encrusted mouldic porosity of algae (eucaryota), cyanobacteria (procaryota) and bryophyte moss (Figures 12 and 13). Traces of fungi may be present but have not been specifically identified. These microbial filaments can be differentiated by the lengths and diameters of the encrusted forms. For example, encrusted algae and cyanobacteria fossils have *ca* 1–2 µm diameters (Figure 13A,B) in contrast with larger diameters, tens to hundreds of microns, of bryophyte sheaths (Figure 13C,D). Tubular form structures of microbial sheaths consist of concentric layers of encrusted calcium carbonate with variously combined polymorphs of ACC, ACC-MHC and CC, interpreted from XRD, SEM and petrographic imaging of fabric textures (Figures 9 through 14).

The size, individual morphometric and cluster arrangements of ACC precipitate of the Wolfenden tufa fabrics are comparable to synthetic ACC precipitates (Avaro et al., 2019; Schmidt et al., 2014). Naturally occurring deposits of ACC spheroids are also recognised in hot spring tufa deposits (Jones & Peng, 2012). The encrusted surfaces of these microbial organisms resulted from the precipitation of ultra-thin laminar precipitates that are smooth in some areas but generally pass into areas consisting of nanoscale aggregates of ACC spheroids with *ca* 50–100 nm diameters. Partially coalesced arrays of these ACC spheroids and other polymorphs accumulate as concentric growth layers with variable surface and internal textures (Figure 14A). The outermost layer or two of these encrustations are characteristically covered by EPS filaments and mixtures of ACC (Figure 14A), MHC (Figure 14B) and CC (Figures 12 and 13).

Nanocrystalline and mesocrystalline textures MHC transformation (ACC-MHC) is associated with the development of 0.2–0.5 µm diameter bulbous protuberances that widely formed on the external surfaces of the

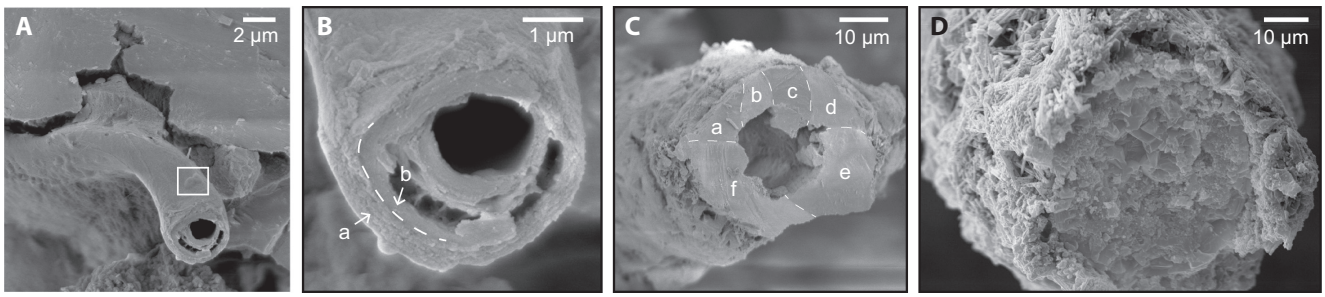

FIGURE 13 Polymorph mineralogy and interior architecture of an encrusted cyanobacteria (A and B) and bryophyte sheaths (C and D) illustrated by SEM imaging. Concentric growth layers consist of amorphous calcium carbonate (ACC)—monohydrocalcite (MHC)—calcite (CC) polymorph transformations. (A) Exterior surface of calcium carbonate precipitation controlled by distribution of EPS nanoscale filaments that provided nucleation sites for precipitation of ACC nanospheroids. Partial ACC-MHC transformation resulted in development of ACC-MHC protuberances (frame). (B) Ultra-structure of concentric growth layers that encrust the microbial sheath. The surface is covered with ACC-coated EPS filaments. Progressive dehydration of the outer growth layer (arrow-a) resulted in an interior nanogranular textured fabric of ACC and mesocrystalline aggregates of the MHC transformation polymorph. Continued dehydration further altered the inner growth layer (arrow-b) with the transformation of ACC-MHC to nanocrystalline calcite. (C) Recrystallisation coalesced nanocrystalline calcite, resulting in micrite or microcrystalline spar sub-domains (a–f). (D) Bryophyte sheath with exterior surface covered by mixture of needle calcite, calcified EPS filaments, ACC-MHC spheroids and calcite platelets. Axial-length mouldic porosity occluded by spar.

encrustations (Figures 12, 13 and 14). The nanoscale ACC-MHC and MHC-CC transformations are recognisable on the surface textures of ACC and ACC-MHC protuberances (Figure 12). The mesocrystalline mosaics consist of interlocking brickwork of anhedral MHC with partial transformation to incipient rhombic crystal faces (Figure 12C, frame). The interiors of these concentric growth layers developed nanogranular textures with mixtures of ACC and MHC. The internal architecture of these concentric growth layers display progressive transformation of ACC to MHC (Figure 13). The outer laminar layers consist of mixtures of ACC precipitate and semi-crystalline nanogranular aggregates of ACC wrapping around mesocrystalline MHC structures (Figure 13Ba). Polymorph transformations occur progressively inward toward the innermost concentric growth layer. This results in the oldest and innermost concentric growth layers consisting of only nanocrystalline micrite (Figure 13Bb). Recrystallisation results in microspar domains (Figure 13Ca through f), which rarely occludes the mouldic porosity of a sheaths (Figure 13D).

Interpretation: The calcium carbonate precipitates initially accumulated as laminar deposits consisting of nanoparticles and nanospheroids of ACC nucleated on microbial EPS substrates (Figure 10). This process resulted in concentric growth layers of calcium carbonate precipitate (Figures 13B and 12C arrow-a). Partial transformation of the ACC to aggregates of ACC-MHC is consistent with XRD analyses. Vaterite at concentration levels below the XRD detection limit may also have been involved in this ACC transformation. This ACC-MHC transformation on and within the outermost concentric growth layers encrusting microbial filaments resulted in nanogranular rice-grain textures (Figure 13Ba). Concentrations of nanocrystalline MHC passed into larger mesocrystalline ultrastructures within the bulbous protuberances emanating outward from the ACC-MHC encrustation (Figure 12). The surfaces of these globular protuberances display polygon brickwork mosaics of interlocking MHC crystalline forms (Figure 12C, frame). These MHC mesocrystal structures transform into CC nanocrystals as the dehydration progressed further (Figure 14B). These are recognisable as rhombic outlines on the surfaces of the globular protuberances. Clusters of MHC nanocrystals are also observed on many encrustation surfaces of microbial sheaths.

6.6 | Stable isotope chemistry

Table 2 records the stable oxygen and carbon isotope values for 27 samples: (1) $\delta^{13}C$ (VPDB) range of −7‰ to −5‰; (2) $\delta^{18}O$ (VSMOW) range of 12‰ to 13‰; (3) $\delta^{18}O$ (VPDB) range of −17‰ to −16‰. The narrow range of these isotope values is consistent with earlier work by Rainey (2009) with only a few samples measured. Measurements of the calcite from the cooler springs such the Wolfenden and Hot Creek tufa deposits have high $\delta^{18}O$ (VSMOW) and low $\delta^{13}C$ (VPDB) values.

6.7 | Bryophyte charcoal and ^{14}C age

A single specimen of tufa was collected with preservation of the pith of bryophyte debris as fragments of charcoal

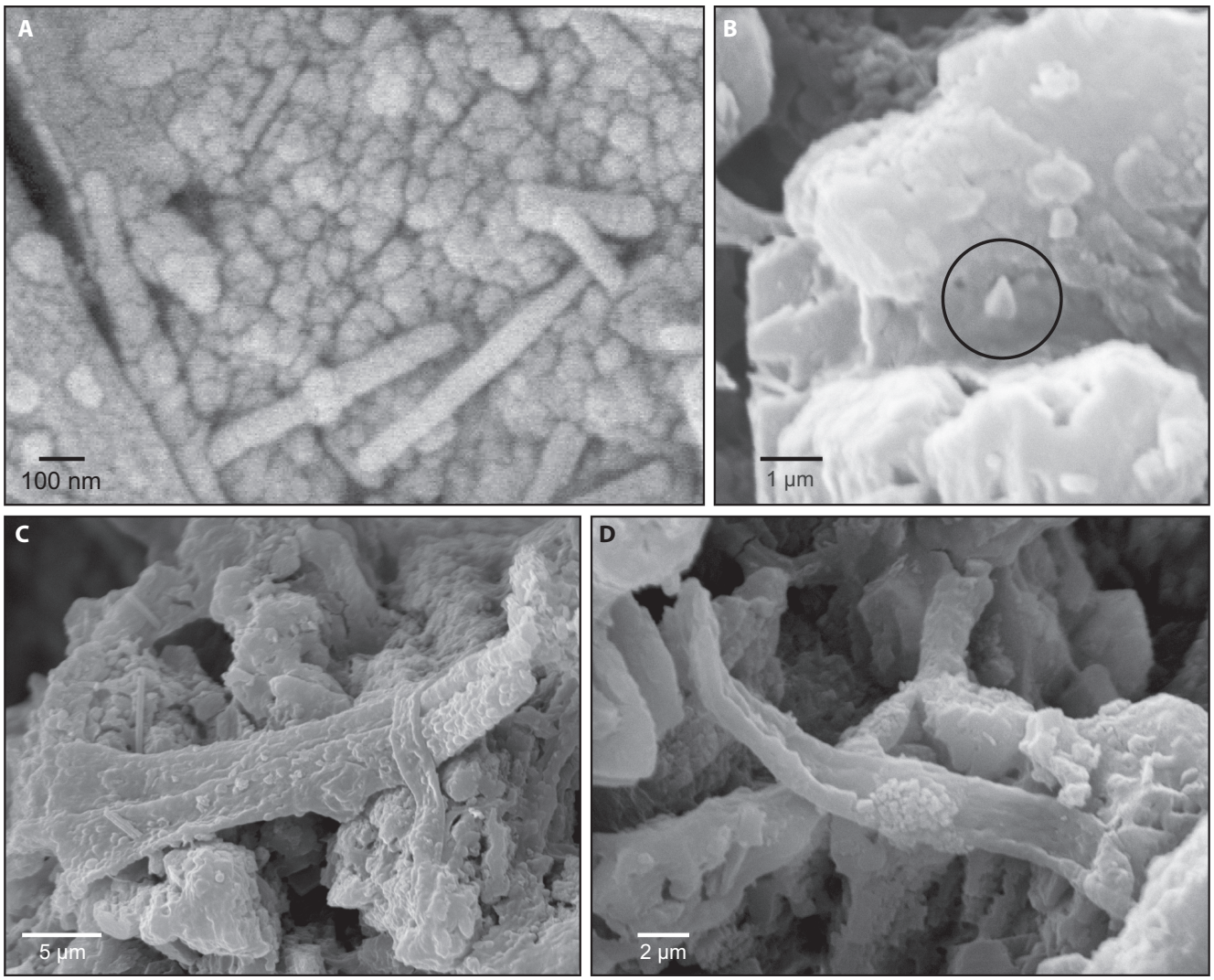

FIGURE 14 SEM imaging of the nanoscale amorphous calcium carbonate transformation to monohydrocalcite. (A) Partially coalesced arrays of EPS-mediated ACC spheroids. (B) Development within a biofilm of a 0.4 μm nanocrystal of monohydrocalcite (circle) on calcite substrate. (C and D) Surface a collapse flattened bryophyte with precipitate of amorphous calcium carbonate partially transformed to monohydrocalcite. (C) Surface covered with nanocrystalline MHC and incipient ACC-MHC protuberances and coalesced calcite platelets. (D) Collapse-curled sheath with surface covering aggregates of nanocrystalline MHC.

(Figure 4), in contrast with the complete decay and formation of mouldic porosity observed elsewhere. This singular specimen also preserved numerous small (*ca* mm) disseminated charcoal particles. The charred bryophyte specimen is comparable to preservation of charred bryophyte remnants at the Fall Creek tufa deposit (Rainey & Jones, 2007). The specimen was suitable for ^{14}C age determination. The sample was ^{14}C dated to 2161 (±38) years BP. The calibration curves indicate 2309–2221 years BP (35.1%); 2215–2191 years BP (3.4%); 2185–2041 years BP (53.3%); 2026–2003 years BP (3.7%).

Interpretation: This charcoal-laden specimen was not collected in situ, but was sampled from a displaced block of tufa situated *ca* 1 m below the upper rim of the covered quarry face. The specimen may have had only minimal dislocation from a possible original position near the top of the deposit, but this is uncertain. The age date of the sample may represent an interval towards the close of the tufa deposition history. It is possible that the 7 m thickness of the tufa deposit represents accumulation during an interval from 4500 to 2000 years BP at an approximate deposition rate of 0.3 cm per year.

7 | DISCUSSION

The ACC-MHC transformation necessarily occurs at lower ambient temperatures characteristic of cooler water tufa deposits (Kimura & Koga, 2011; Nishiyama et al., 2013; Wang et al., 2015). In contrast, direct ACC-CC

TABLE 2 Stable isotope data of the Wolfenden tufa

Sample	$\delta^{13}C$ VPDB (‰)	$\delta^{18}O$ VSMOW(‰)	$\delta^{18}O$ VPDB (‰)	Sample	$\delta^{13}C$ VPDB (‰)	$\delta^{18}O$ VSMOW (‰)	$\delta^{18}O$ VPDB (‰)
1	−6.0	13.1	−17.3	15	−5.8	13.1	−17.2
2	−6.9	13.0	−17.4	16	−5.5	12.8	−17.6
3	−6.4	13.7	−16.7	17	−6.4	13.5	−16.9
4	−7.1	13.4	−17.0	18	−6.3	13.5	−16.9
5	−6.9	12.4	−17.9	19	−7.0	13.2	−17.2
6	−5.8	13.5	−16.9	20	−6.5	13.0	−17.4
7	−5.3	12.8	−17.6	21	−6.5	12.7	−17.7
8	−6.7	13.2	−17.2	22	−6.4	12.9	−17.5
9	−5.4	13.3	−17.1	23	−6.6	12.8	−17.6
10	−5.9	13.2	−17.2	24	−6.1	13.1	−17.3
11	−6.5	13.3	−17.1	25	−5.0	12.7	−17.7
12	−6.0	13.7	−16.7	26	−6.7	12.8	−17.6
13	−6.9	13.2	−17.2	27	−7.2	13.1	−17.3
14	−6.6	12.8	−17.6				

transformation can occur at more elevated temperatures, as documented in hot spring tufa and travertine deposits (Jones & Peng, 2012). Stable carbon and oxygen isotope analyses of calcite have been used to provide insights into the extent to which organisms, particularly cyanobacteria, have removed dissolved carbon dioxide and thereby trigger biotic calcium carbonate precipitation, in contrast to abiotic precipitation in supersaturated water triggered by rapid degassing.

Isotope chemistry is useful to distinguish between hydrothermal, karstic freshwater, and evaporative lake carbonate deposits (Della Porta, 2015). The isotope values indicate responsiveness to a meteoric charged groundwater having a consistent chemistry throughout the tufa deposition. Distribution of $\delta^{18}O$ and $\delta^{13}C$ isotope values can be used to broadly differentiate thermal water deposits of tufa/travertine from colder water tufa deposits (Gandin & Capezzuoli, 2008; Rainey, 2009). Stable carbon and oxygen isotope signatures can provide recognisable linkages to parent water source systems by providing signatures useful to differentiate cold water tufa from elevated water temperatures of hot spring deposits sourced from deeply circulated groundwater along fault systems and responsive to the geothermal gradient. These hot spring water systems have the capacity for supersaturation and retain relatively high levels of soluble minerals. Upon exposure to atmospheric conditions at the surface, rapid and intense degassing triggers abiotic deposition of calcium carbonate as hot springs tufa or travertine. In contrast, calcium carbonate deposits from cold water springs result in tufa with differing sets of isotope values responsive to microbial processes in contrast to calcium carbonate precipitation triggered by degassing. The isotope data suggest that most travertine calcite precipitation resulting from abiotic degassing record ranges of positive $\delta^{13}C$ (VPDB) values, but with negative to strongly negative $\delta^{18}O$ (VPDB) values. In contrast, shallow cold spring water tufa deposits record isotope signatures with negative $\delta^{18}O$ values and markedly negative ranges of $\delta^{13}C$ values, such as those recorded for the Wolfenden tufa (Table 2).

7.1 | ACC transformation to crystalline polymorphs

There is widespread interest on the extent that nanoparticulate ACC occurs as a precursor to the more crystalline polymorphs in both marine and non-marine depositional environments. ACC, a calcium-rich hydrated molecular structure, is thermodynamically unstable as a pure chemical compound. There is some evidence that ACC is not amorphous sensu stricto (Rez et al., 2014). The structure includes nanoscale (*ca* 1.0 nm) needle and rhomb-shaped crystals, but random orientation result in the absence of optical birefringence. ACC is more stable when the molecular structure has been altered by adsorption of organic compounds or metallic ions such as Mg (Addadi et al., 2003; Lyu et al., 2020; Mass et al., 2017; Obst et al., 2009; Weiner et al., 2003). The incorporation of organic molecules into the ACC molecular structure can result in insoluble and stabilised molecular structures. Stable forms of ACC are widely produced during biomineralisation by marine life forms because of the interference by organic molecules (Meldrum, 2003; Weiner et al., 2003). Most research has focused on marine biominerisation processes by which aragonite is fixed by marine

organisms as skeletal, exoskeletal or shell structures (Addadi et al., 2003; Politi et al., 2004). Marine biomineral transformations of biogenic ACC to more crystalline calcium carbonate polymorphs, mostly aragonite, do not involve the formation of MHC or vaterite as an intermediate transformational stage (Albéric et al., 2018; Goodwin et al., 2010; Loste et al., 2003; Mass et al., 2017; Ogino et al., 1987; Rodriguez-Blanco et al., 2011). Similarly, synthetic calcite can be experimentally derived from stabilised ACC by the presence of EPS or other organic compounds.

The precipitation of ACC is attributed to either of two nucleation mechanisms. The classic model assumes that biogenic ACC nucleates and expands with ion adsorption (Cölfen & Mann, 2003; Mann et al., 1988), which permits a level of molecular stability in contrast to the instability of very pure ACC. Increasing levels of Mg^{2+} in ACC increase its stability, as does increased levels of EPS-derived and other organic compounds. A rival biomineral model proposes that calcium carbonate can be formed as stable pre-nucleation stage clusters with aggradation into an ACC phase by colliding and coalescing and then transforming into a crystalline phase (Gebauer et al., 2008). Dupraz et al. (2009) has proposed a multi-step process model for ACC precipitation. This process is initiated by local increases in alkalinity and pockets of supersaturation within the micro-domains of EPS (Decho, 2010; Dupraz et al., 2004, 2009; Zavarin, 2002). The formation of an ACC gel follows, resulting in the morphogenesis of nanospheres of ACC and acidic EPS macromolecules. The EPS-laden biofilms represent a collection of organic molecules known to interfere with crystallographic structures of calcium carbonate and result in transformation of ACC into MHC (Wang et al., 2015). The EPS matrix is gradually replaced and calcified by nanospheres of ACC, which seed further crystallisation. The ACC transformation occurs on substrates of EPS, resulting in indirect transformation to CC, subsequent to formation of MHC with progressive dehydration. ACC forms on the surface of the microbial filaments in low alkalinity depositional environments as a protective mechanism against uncontrolled precipitation of thermodynamically stable calcite, which would result in entombment and mortality of the organisms (Banfield et al., 2000; De Stasio et al., 2005; Konhauser et al., 1993).

Marine biomineralisation may involve facilitation of a biofilm EPS matrix for the transformation of ACC to $CaCO_3$ polymorphs in addition to the dominant and pervasive role of Mg adsorption (Kimura & Koga, 2011; Loste et al., 2003). For example, the formation of ooids and early marine cement involved microbial-mediated organomineralisation that included EPS fixation of ACC as precursor to aragonite crystallisation at locations in the Bahamas (Diaz et al., 2017; Diaz & Eberli, 2019). The concentration of Mg ions in oceanic water facilitates this biomineralisation by marine organisms for the direct transformation of ACC to aragonite. It is recognised that very pure ACC can directly crystallise to vaterite or calcite, but the effect of Mg^{2+} on the calcium carbonate structure can drive the selection of the polymorph mineralogy such as aragonite in sea water. In contrast, there is a general lack of research available on microbial EPS-mediated ACC transformation to more crystalline polymorphs such as MHC or vaterite in fresh water depositional environments. Calcium carbonate in the natural environment occurs in non-crystalline and crystalline polymorphs (Meldrum, 2003; Radha et al., 2010), represented mostly by calcite and aragonite and comparatively rare occurrences of amorphous forms (ACC), MHC and vaterite.

The extent to which MHC is the definitive intermediate form in the transformation between ACC and CC ancient and modern non-marine depositional environments remains uncertain, and the crystallisation mechanisms are poorly understood (Rodriguez-Blanco et al., 2014). The presence of the kinetically metastable MHC or the vaterite polymorph has been documented for non-marine deposits (Swainson, 2008), but is rare. The precipitation of MHC may be fundamental as the intermediate transitory stage between ACC and calcite nanocrystallisation in continental deposits but this is uncertain, unlike direct ACC-aragonite/calcite transformation by marine organisms without intermediary polymorphs. As such, the precipitation of ACC and subsequent ACC-MHC transformation in non-marine deposits would be responsive to microbial EPS-mediated production of ultra-thin laminar biofilms characterised by the production of EPS filaments. Floating meshworks of EPS filaments can be anchored by a filamentous biofilm (Janissen et al., 2015), such as examples from the Wolfenden tufa (Figure 10). It is widely recognised that organic inhibitors such as EPS can result in well-developed arrays of ACC spheroids and further facilitate the temporal stability (Rodriguez-Navarro et al., 2007; Xu et al., 2004). The EPS-laden biofilms provide functional stability for unstable phases such as biofilm-induced nanoparticle nucleation of ACC. Unusually high concentrations of EPS molecules favoured the adsorption of organic molecules into the ACC, resulting in the preservation of this unstable polymorph. Nonetheless, progressive dehydration resulted in transformation into and preservation of MHC, and eventually micrite (Figure 14).

The concentrated adsorption of magnesium in the Wolfenden tufa is interpreted to have resulted in the morphogenesis of needle calcite directly from the ACC precipitate without involving an ACC-MHC transformation. Research by Rodriguez-Blanco et al. (Rodriguez-Blanco et al., 2014, 2015, 2012) indicates that lower levels of Mg^{2+} such as 10% results in Mg-calcite. Levels of *ca* 30% Mg^{2+} result in MHC and as much as 50% Mg^{2+} results in proto-dolomite. Some

evidence indicates that the presence of Mg^{2+} can also result in formation of MHC with stabilisation by organic compounds in non-marine deposits (Pan et al., 2019). Models have been developed for some Mg-calcite and aragonite deposits in the geologic record having been originally formed with a metastable MHC precursor (Nishiyama et al., 2013; Rodriguez-Blanco et al., 2014). These levels of magnesium are more relevant to the formation of Mg-calcite and MHC in saline lakes. This morphogenesis and geochemistry are not comparable to the moderately low magnesium concentration during accumulation of the Wolfenden tufa. Nonetheless, the levels of magnesium would have been sufficient to trigger the formation of needle calcite crystal habits in association with biofilm.

7.2 | Carbonate precipitation model

Research on the Wolfenden tufa supports the interpretation that non-marine transformation of ACC precipitate to crystalline polymorphs in tufa is essentially a biofilm EPS-mediated nucleation process without Mg adsorption, but necessarily involves the formation of a transitional polymorph (ACC, MHC) as precursors to calcite nucleation. In non-marine deposits, EPS and related organic molecular structures substitute for magnesium in the determination of the calcium carbonate polymorph and the crystalline habit. There is only sparse research available on ACC-MHC transformations as precursor to nanocrystal nucleation of naturally occurring calcite. It is the EPS and related organic molecules that mediate the ACC precipitation, not the direct fixation by microbe cells. This microbial process in the Wolfenden tufa is not biomineralisation, sensu stricto, resulting from metabolic activity of the microbe cellular structure such as during sulphate reduction or photosynthesis (Della Porta et al., 2022; Konhauser, 1993, 1997, 1998; Reitner et al., 1997).

Production of ACC results from responsiveness to nucleation sites on a biofilm EPS matrix. Incipient ACC precipitation at the nanoscale follows at nucleation sites on the EPS matrix (Lyu et al., 2020). This process occurs at the nanoscale as EPS-mediated processes (Rodriguez-Blanco et al., 2011; Rodriguez-Navarro et al., 2007). It is also experimentally recognised that precipitation of MHC (or vaterite) nanoparticles can be triggered by localised supersaturation microenvironments associated with EPS from microbial activity (Konrad et al., 2018; Lyu et al., 2021; Rodriguez-Blanco et al., 2014; Rodriguez-Navarro et al., 2007; Wang et al., 2015). Experimental evidence provided by synthetic preparations of calcite has demonstrated that dehydration of the ACC structural ordering leads to the formation of the larger spheroidal aggradations of crystalline structures.

The Wolfenden tufa provides evidence for the pervasive formation and distribution of EPS-ACC deposits on the exterior surfaces of the cyanobacteria, algae, and flora such as bryophyte moss. These concentric growth layers consist of arrays of partially coalesced nanoscale spheroids of ACC (Figures 10 and 14A) and mesogranular aggregates of ACC-MHC (Figure 14) associated with the pervasive distribution of EPS filaments. The ACC and MHC nanostructures developed as 400–800 nm long bulbous protuberances. These elongated spheroidal protuberances have sizes comparable to nanoparticle aggradation of experimental ACC-MHC precipitate documented by Konrad et al. (2018). The widely distributed protuberances exhibit evidence of multiple polymorph transformations (Figure 12). This is observed as the development of faint outlines of incipient calcite crystal faces representing solid state transformation within the MHC mesocrystalline interior structure of these ACC protuberances (Figure 12C, inset arrow-b). A similar transformation occurs inward within the concentric growth layers of ACC-MHC, resulting in an ACC-MHC-CC transformation sequencing of the substrate (Figure 13B). Transformation into micrite fabrics as the singular mineralogy follows within the inner concentric layers. A complete transformation of ACC-MHC to CC and eventually to micrite and microspar fabrics results from recrystallisation (Figure 13C). All evidence of precursor ACC precipitation and transformation to MHC may be obliterated.

This research on the Wolfenden tufa fabrics documents the first observational evidence of precursor ACC-MHC polymorph precipitation and transformation during early tufa deposition. In contrast, more advanced stages of this process resulting in CC have been recognised in other western Canadian tufa deposits such as the Hot Creek tufa (Rainey & Jones, 2010) and the Big Hill Springs tufa (Turner & Jones, 2005). The mechanism that facilitated but also preserved evidence of these incomplete transformations by stabilising calcium carbonate polymorphs at different transformation stages was the overabundance of ESP adsorption that permitted responsiveness to ACC nucleation.

The calcium carbonate polymorph transformation sequencing is recognised as a 4-step process (Figure 15):

Step 1: Nucleation of ACC on EPS filaments. Pervasive distribution of microbial EPS-mediated nucleation sites for ACC precipitate results in the encapsulation of the EPS filaments by nanospheroids of ACC. Various levels of molecular stability of the hydrated ACC were responsive to the adsorption of organic molecules into the molecular structure (Lyu et al., 2020; Obst et al., 2009; Radha et al., 2010; Robin et al., 2015). Ultra-thin deposits of ACC-coated EPS filaments formed and developed as growth layers on the surfaces of cyanobacteria, bryophytes and other organisms.

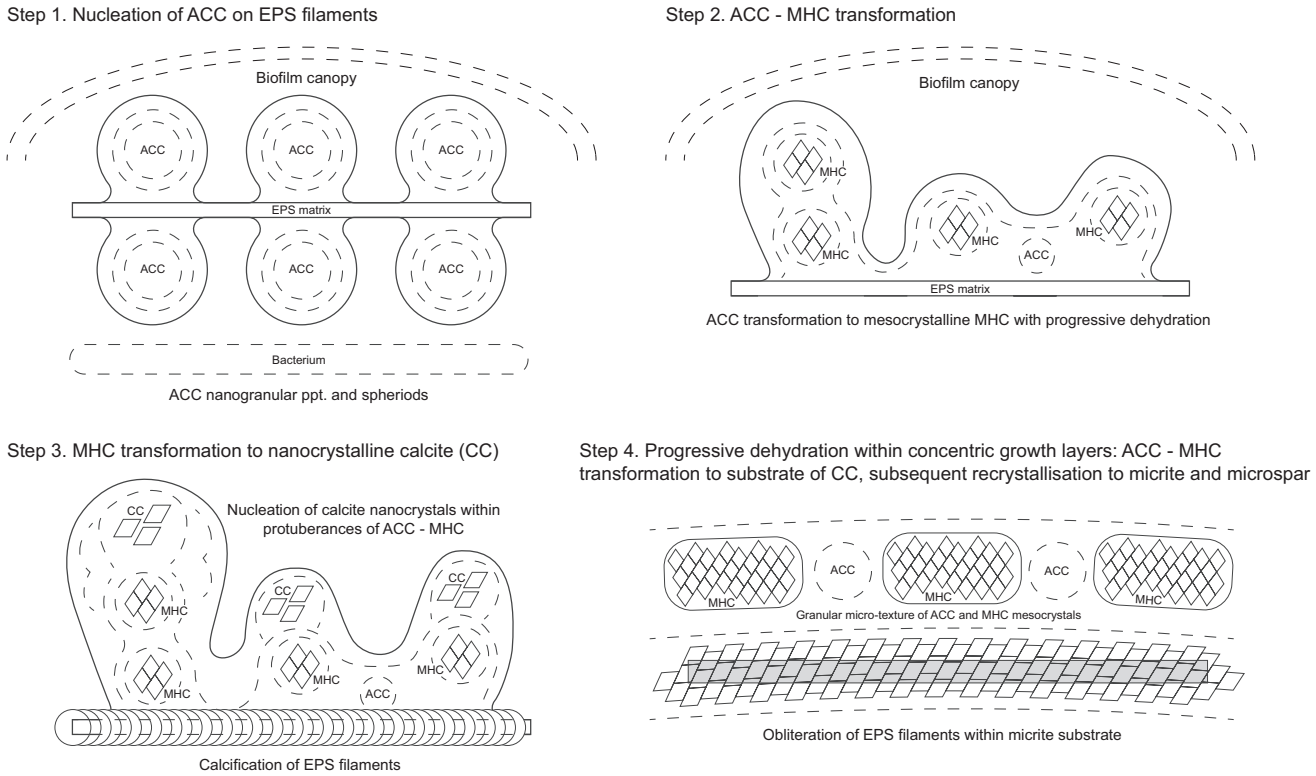

FIGURE 15 Model of the 4-step calcium carbonate polymorphs transformation process of the Wolfenden tufa resulting from biofilm EPS-mediated nucleation of hydrated amorphous calcium carbonate. Progressive dehydration in the concentric growth layers resulted in a precursor ACC-MHC transformation mineralogy and eventually widespread formation of nanocrystalline calcite and calcification of the EPS filaments.

Step 2: ACC-MHC transformation. Stabilisation of the ACC precipitate was responsive to the adsorption of EPS-linked organic molecules, but further dehydration resulted in ACC transformation to MHC. Additional adsorption resulted in stabilised mixtures of ACC and MHC. Concentric layers of ACC that encrusted the EPS filaments and larger areas such as surfaces of algae, cyanobacteria and flora were transformed into ACC-MHC, characterised by mottled rice-grain textures consisting of mesocrystalline MHC structures within the concentric EPS-ACC growth layers. The enlargement of these MHC mesocrystalline structures triggered development of elongated protuberances consisting of ACC-MHC (Figure 12). The protuberances lengthened as the transformation to ACC-MHC progressed, resulting in the partial to complete fragmentation of overlying EPS-ACC crusts on the microbial sheaths (Figure 12C, arrow-a).

Step 3: MHC-CC transformation. The MHC within the ACC-MHC growth layers partially transformed to nanoscale calcite with continued crystallographic dehydration. Rhombic crystal faces of CC are recognisable on surfaces of the ACC-MHC protuberances (Figure 12C frame). These protuberances expand and coalesce into a new concentric growth layer. The concentric layered substrates of nanogranular ACC-MHC similarly transform into layers of nanoscale CC and micrite (Figure 13Ba→b).

Step 4: Transformation and recrystallisation. Progressive transformation of ACC-MHC occurred inwardly layer-by-layer, resulting in a nanocrystalline and micrite fabric. Recrystallisation obliterated all evidence of calcified EPS filaments in the substrate. Many growth layers of micrite recrystallised as spar (Figure 13C,D).

8 | WOLFENDEN AND OTHER WESTERN CANADIAN TUFA DEPOSITS COMPARED

Tufa deposits located in the mountainous terrains of the eastern Cordillera of western Canada consist of calcium carbonate precipitates that encrust algae, cyanobacteria and larger flora such as bryophyte moss. The calcite fabrics were responsive to water chemistry and temperature variability, and differ from deposit to deposit. The depositional conditions were responsive to: (1) chemistry of the dissolved solids and level of carbonate saturation responsive to the rate and extent of carbonate bedrock dissolution by groundwater; (2) seasonal temperature range of spring water flow and rate of CO_2 degassing; (3) floral assemblage and microbial activity. Each deposit has distinct assemblages of lithofabric and petrofabric characteristics

because of variable organic debris within a range of groundwater chemistry and atmospheric conditions.

The concentration of bryophyte debris in the Wolfenden tufa, now represented by tubular mouldic porosity, is comparable with a few other tufa deposits in the eastern Rocky Mountains and foothills. For example, the Fall Creek tufa deposit in south-west Alberta (Figure 1) similarly accumulated a concentration of encrusted bryophytes, identified as *Cratoneuron commutatum* by Rainey and Jones (2007). There is also possible taxonomic similarity with bryophytes identified at the nearby Hot Creek tufa deposit (Rainey, 2009; Rainey & Jones, 2010).

The Hot Creek tufa deposit has also been interpreted by Turner and Jones (2005) to have evidence of ACC-calcite transformation (Figure 1). This interpretation lacks the recognition of an intermediate polymorph transformation stage such as MHC or vaterite. It interprets a somewhat more advanced aspect of an early precipitation stage with the micro-fabrics represented by sheets composed of crystal face arrays that replaced the ACC precipitate. In contrast, the Wolfenden tufa provides a unique insight into an even earlier precursor stage that resulted in the ACC-MHC transformation, and records the ACC-MHC-CC transformation sequence on surfaces of algae, cyanobacteria and bryophytes, now calcified fossils.

Selected tufa deposits in the eastern Cordillera are compared to the Wolfenden deposit, presenting an overview of similarities and contrasts.

8.1 | South-Eastern British Columbia

8.1.1 | Hot Creek

The tufa deposit is as much as 3 m thick at a site a few kilometres to the north-west of the Wolfenden tufa deposit along the eastern margin of the Rocky Mountain Trench (Figure 1). The Hot Creek tufa is essentially a cyanobacteria-dominated deposit (Rainey, 2009; Rainey & Jones, 2010), in contrast to the algae and bryophyte-dominated Wolfenden tufa. Charcoal embedded in the Hot Creek tufa record ^{14}C dates of 7327 years BP to 7432 years BP, and 6677 BP to 6790 years BP (Rainey, 2009; Rainey & Jones, 2010). Wood samples collected from the younger, downslope, distal portion of the tufa record dates of 1070 years BP to 1340 years BP and 570 years BP to 730 years BP. The Hot Creek petrofabrics indicate an ACC precursor fabric that records a more advanced development stage compared to the Wolfenden tufa. Rainey and Jones (2010) record evidence that the nanoscale faces of calcite crystals indicate a precursor ACC precipitate. This ultra-structure fabric consists of arrays of partially coalesced nanocrystalline terminations aligned on cyanobacterial sheaths.

8.1.2 | Fairmont

The thermal spring deposit at Fairmont is one of the most widely studied in western Canada. It consists of a lower interval of biotic tufa and an overlying interval of mixed biotic–abiotic travertine (Rainey, 2009; Rainey & Jones, 2009). The lower tufa interval is a macrophyte facies of calcite encrusted plant debris, resulting in a pervasive mouldic porosity. The interval includes a widely distributed stromatolite facies with associated microbial filaments and bubble fabrics. The stromatolite intervals are as much as 2 m thick, and consist of multiple millimetre-thick sheets of CC encrustations. Calcite-encrusted microbial filaments, 20–50 μm long and 5–10 μm wide, have the sheath structures occluded by cement. The bubble fabrics consist of calcite encrusted spherical voids with 1–5 mm diameters. The overlying travertine interval is characterised by abiotic dendritic feather-form shrub fabrics. Charcoal ^{14}C dates indicate that the tufa accumulated during the early Holocene from 6600 years BP to 8800 years BP (Rainey & Jones, 2009).

8.2 | South-Western Alberta

8.2.1 | Fall creek

The flora of the Fall Creek cold water tufa in south-western Alberta is comparable to that of the Wolfenden tufa. The calcite fabrics are characterised by extensive recrystallisation of encrusted bryophytes, masking but not entirely obliterating earlier fabrics. The tufa deposit is also the site of a modern stream that does not currently precipitate calcium carbonate, unlike the modern stream near the Wolfenden tufa deposit. At Fall Creek, the moss *Cratoneuron* sp. accumulates on a calcium-rich substrate of the modern stream. The δ^{18}O (VPDB) data record a range of −18‰ to −17‰, and δ^{13}C (VPDB) data record a range of −1.2‰ to +0.5‰. The isotope data indicate that the carbonate deposition remained in isotopic equilibrium during carbonate precipitation (Rainey & Jones, 2007). Radiocarbon dating of the youngest part of the tufa deposit indicates an age of only 310 years BP (±50), but deposition may have started as much as 5000 years BP, concurrent with deposition at the Cave and Basin Hot Spring deposit at Banff, Alberta.

8.2.2 | Miette

A cluster of active hot springs is located within the Jasper National Park in south-western Alberta. The area includes a relict tufa deposit extending for 500 m along

the valley wall of Sulphur Creek (Bonny, 2002; Bonny & Jones, 2003a, 2003b). The tufa depositional surfaces along the divergent valley wall slopes resulted in various dome and roll-over deposits as well as horizontal, inclined and wedge-shaped deposit facies (Bonny & Jones, 2003a, 2003b). The tufa floral debris consists mostly of hummocky bryophyte mosses comparable to the Wolfenden tufa, resulting in calcite encrustations and replacement fabrics. Bison bone fragments within the tufa have been ^{14}C dated at 2350 to 2025 years BP. The stratigraphic position of these bones suggests that the spring flow from about 4500 years BP to 2500 years BP. This timeframe correlates with the onset of cooler and moist climate conditions that started about 5000 years BP across the eastern plains of the Rockies (Osborn & Luckman, 1988; Bonny & Jones, 2003a, 2003b). The age of the Miette tufa may be comparable to the time span of the Wolfenden tufa deposit.

8.2.3 | Big Hill Springs

The tufa deposit accumulated along a spring emanating from calcareous sandstones of the Pasakapoo Formation (Palaeocene). The deposit accumulated as a 110 m wide and 6 m high tufa barricade complex (Turner & Jones, 2005). It is characterised by calcified hummocky bryophyte mounds comparable to the flora of the Wolfenden tufa. Various breach points resulted in cascaded stream flows characterised by spray zones, which are environments favourable for growth of hummocky bryophyte mounds. Carbonate deposition continues to this day in splash zones of the active stream, where cyanobacterial growths accumulate on cobbles and other surfaces.

9 | CONCLUSIONS

There is an increased awareness that the microbial EPS-mediation of calcium carbonate precipitation in tufa deposits involved the nucleation and preservation of ACC as a precursor polymorph. Observations of this process have been associated mostly with hot spring deposits but also in some cold water tufa and other non-marine environments. Progressive dehydration of the ACC molecule results in solid state transformation into MHC or vaterite polymorphs characterised by intermediate thermodynamic and kinetic stabilities, prior to transformation to calcite. Some deposits elsewhere preserve the precursor ACC precipitate, but no other preserves evidence of the ACC-MHC transformation. The Wolfenden tufa deposit is unique in that it records the complete ACC-MHC-CC transformation sequence and each stage of the solid state transformation sequence as a precursor fabric. The unique preservation of the ACC-MHC-CC transformation sequencing at the Wolfenden tufa resulted from the unusual and pervasive oversupply of EPS filaments, resulting in the stabilisation and preservation of ACC transformation polymorphs by EPS-mediated organic molecules having been adsorbed into the ACC molecular structure.

The Wolfenden tufa provides the opportunity to observe snapshots of this early carbonate precipitation process in contrast to having been masked or obscured by more advanced stages of tufa deposition represented by calcite encrusted biota and development of mouldic porosity. Tufa deposits worldwide are widely recognised as calcite cement fabrics that encrusted floral debris, followed by extensive developments of mouldic porosity upon organic decay. As such, only the calcite polymorph has been generally considered as the mineralogy for the entire depositional process, and other calcium carbonate polymorphs as precursors to ubiquitous calcite precipitation have not been routinely investigated. In contrast, the Wolfenden tufa provides insights into the earliest precipitation processes prior to widespread calcite cementation that results in calcite encrustation textures. This ACC-MHC-CC transformation sequencing at the Wolfenden tufa is a plausible general case for other tufa deposits worldwide, including deposits where the evidence for the earliest carbonate precipitation process has been obliterated by recrystallisation or the nanoscale nucleation process overlooked.

ACKNOWLEDGEMENTS

This research includes SEM images provided with permission but without commentary by D. K. Rainey of study material obtained during active quarry operations, but not used for research on tufa deposits in western Canada (Rainey, 2009; Rainey, personal communication, 2021). SEM images of this material, albeit without description, stratigraphic position or interpretation, have been kindly provided by Dr. D. Rainey for use in this research. The author acknowledges the cooperation of the land owner providing permission to enter the Brisco Quarry and collect samples. Isotope values were provided by Dr. Stephen Taylor, Isotope Lab of the Department of Earth Sciences, University of Calgary. XRD analyses were provided by the Calgary facilities of the AGAT Laboratory and Calgary Rock and Materials Services. Thin-sections and additional SEM images were prepared at the facilities of Calgary Rock and Material Services. 14C age dates were provided by the André E. Lalonde AMS Laboratory, University of Ottawa. The author gratefully acknowledges the invaluable commentaries by Prof. G. Della Porta, University of Milan, and anonymous reviewers. The author also gratefully acknowledges the editorial contribution by the

Associate Editor, Dr. James Klaus, and manuscript editing by Greta Mackenzie. Open access funding enabled and organized by ProjektDEAL.

CONFLICT OF INTEREST

The author declares that this research was conducted in the absence of any commercial or financial relationships that could be construed as a potential conflict of interest. This research has been privately funded by the author.

DATA AVAILABILITY STATEMENT

There are no supplemental data files.

ORCID

Paul L. Broughton https://orcid.org/0000-0002-8285-0556

REFERENCES

Addadi, L., Raz, S. & Weiner, S. (2003) Taking advantage of disorder: amorphous calcium carbonate and its roles in biomineralization. *Advanced Materials*, *15*(12), 959–970. https://doi.org/10.1002/adma.200300381

Albéric, M., Bertinetti, L., Zou, Z., Fratzl, P., Habraken, W. & Politi, Y. (2018) The crystallization of amorphous calcium carbonate is kinetically governed by ion impurities and water *Advanced Science*, *5*, 1–9. https://doi.org/10.1002/advs.201701000.

Allen, D.M., Grasby, S.E. & Voormeij, D.A. (2006) Determining the circulation depth of thermal springs in the southern Rocky Mountain Trench, south-eastern British Columbia, Canada using geothermometry and borehole temperature logs. *Hydrogeology Journal*, *14*, 159–172. https://doi.org/10.1007/s10040-004-0428-z

Avaro, J.T., Ruiz-Agudo, C., Landwehr, E., Hauser, K. & Gebauer, D. (2019) Impurity-free amorphous calcium carbonate, a preferential material for pharmaceutical and medical applications. *European Journal of Mineralogy*, *31*, 231–236. https://doi.org/10.1127/ejm/2019/0031-2831

Banfield, J.F., Welch, S.A., Zhang, H., Ebert, T.T. & Penn, R.L. (2000) Aggregation-based crystal growth and microstructure development in natural iron oxyhydroxide biomineralization products. *Science*, *289*, 751–754. https://doi.org/10.1126/science.289.5480.751

Bonny, S. (2002) Relict tufa at Miette Hot Springs, Jasper National Park, Alberta. MSc Thesis, University of Alberta, Edmonton.

Bonny, S. & Jones, B. (2003a) Relict tufa at Miette Hot Springs, Jasper National Park, Alberta, Canada. *Canadian Journal of Earth Sciences*, *40*(11), 1459–1481. https://doi.org/10.1139/e03-050

Bonny, S. & Jones, B. (2003b) Microbes and mineral precipitation, Miette Hot Springs, Jasper National Park, Alberta, Canada. *Canadian Journal of Earth Sciences*, *40*(11), 1483–1500. https://doi.org/10.1139/e03-060

Borneuf, D. (1983) *Springs of Alberta*. Earth Science Report 82-3. Alberta Research Council, Edmonton, 95 p.

Borsato, A., Frisia, S., Jones, B. & Van der Borg, K. (2000) Calcite moonmilk: crystal morphology and environment of formation in caves in the Italian Alps. *Journal of Sedimentary Research*, *70*(5), 1179–1182.

Bots, P., Benning, L.G., Rodriquez-Blanco, J.-D., Roncal-Herrero, T. & Shaw, S. (2012) Mechanistic insights into the crystallization of amorphous calcium carbonate (ACC). *Crystal Growth & Design*, *12*(7), 3806–3814. https://doi.org/10.1021/cg300676b

Brock, F., Higham, T., Ditchfield, P. & Bronk Ramsey, C. (2010) Current pretreatment methods for AMS radiocarbon dating at the Oxford Radiocarbon Accelerator Unit (ORAU). *Radiocarbon*, *52*(1), 103–112. https://doi.org/10.1017/S0033822200045069

Bronk Ramsey, C. (2009) Bayesian analysis of radiocarbon dates. *Radiocarbon*, *51*(1), 337–360. https://doi.org/10.1017/S0033822200033865

Cailleau, G., Verrecchia, E.P., Braissant, O. & Emmanuel, L. (2009) The biogenic origin of needle fibre calcite. *Sedimentology*, *56*, 1858–1875. https://doi.org/10.1111/j.1365-3091.2009.01060.x

Capezzuoli, E., Gandin, A. & Pedley, M. (2014) Decoding tufa and travertine (fresh water carbonates) in the sedimentary record: the state of the art. *Sedimentology*, *61*, 1–21. https://doi.org/10.1111/sed.12075

Chafetz, H.S. & Folk, R.L. (1984) Travertines: depositional morphology and the bacterially constructed constituents. *Journal of Sedimentary Petrology*, *54*(1), 289–316. https://doi.org/10.1306/212F8404-2B24-11D7-8648000102C1865D

Claes, H., Miranda, T., Falcão, T., Soete, J., Mohammadi, Z., Zieger, L., Erthal, M., Aguillar, J., Schmatz, J., Busch, A. & Swennen, R. (2021) Model for calcite spherulite formation in organic, clay-rich, lacustrine carbonate shales (Barbalha Formation, Aptian, Araripe Basin, NE Brazil). *Marine and Petroleum Geology*, *128*, 1–18. https://doi.org/10.1016/j.marpetgeo.2021.104988.

Cölfen, H. & Mann, S. (2003) Higher-order organization by mesoscale self-assembly and transformation of hybrid nanostructures. *Angewandte Chemie International Edition*, *42*, 2350–2365. https://doi.org/10.1002/anie.200200562

Coney, P.J., Jones, D.L. & Monger, J.W.H. (1980) Cordilleran suspect terranes. *Nature*, *288*, 329–333. https://doi.org/10.1038/288329a0

Coplen, T.B., Kendall, C. & Hopple, J. (1983) Comparison of stable isotope reference samples. *Nature*, *302*, 236–238. https://doi.org/10.1038/302236a0

Crann, C.A., Murseli, S., St-Jean, G., Zhao, X., Clark, I.D. & Kieser, W.E. (2017) First status report on radiocarbon sample preparation techniques at the A.E. Lalonde Laboratory (Ottawa, Ontario). *Radiocarbon*, *59*(3), 695–704. https://doi.org/10.1017/RDC.2016.55

De Stasio, G., Schmitt, M. & Gwellman, S.H. (2005) Spectromicroscopy at the organic-inorganic interface in biominerals. *American Journal of Science*, *305*, 673–686. https://doi.org/10.2475/ajs.305.6-8.673

Decho, A.W. (2010) Overview of biopolymer-induced mineralization: what goes on in biofilms? *Ecological Engineering*, *36*(2), 137–144. https://doi.org/10.1016/j.ecoleng.2009.01.003

Della Porta, G. (2015) Carbonate build-ups in lacustrine, hydrothermal and fluvial settings: comparing depositional geometry, fabric types and geochemical signature. In: Bosence, D., Gibbons, K., Le Heron, D., Morgan, W., Pritchard, T. & Vining, B (Eds.) *Microbial carbonates in space and time: implications for global exploration and production*. London: Geological Society (London), *Special Publication*, *418*, pp. 17–68.

Della Porta, G., Hoppert, M., Hallmann, C., Schneider, D. & Reitner, J. (2022) The influence of microbial mats on travertine

precipitation in active hydrothermal systems (Central Italy). *The Depositional Record*, *8*(1), 165–209. https://doi.org/10.1002/dep2.147

Deng, H., Wang, S., Wang, X., Du, C., Shen, X., Wang, Y. & Cui, F. (2015) Two competitive nucleation mechanisms of calcium carbonate biomineralization in response to surface functionality of low calcium ion concentration solution. *Regenerative Biomaterials*, *2*(3), 187–195. https://doi.org/10.1093/rb/rbv010

Diaz, M.R. & Eberli, G.P. (2019) Decoding the mechanism of formation in marine ooids: a review. *Earth-Science Reviews*, *190*, 536–556. https://doi.org/10.1016/j.earscirev.2018.12.016

Diaz, M.R., Eberli, G.P., Blackwelder, P.L., Phillips, B. & Swart, P.K. (2017) Microbially mediated oranomineralization in the formation of ooids. *Geology*, *45*, 771–774. https://doi.org/10.1130/G39159.1

Dupraz, C., Reid, R.P., Braissant, O., Decho, A.W., Norman, R.S. & Visscher, P.T. (2009) Processes of carbonate precipitation in modern microbial mats. *Earth-Science Reviews*, *96*, 141–162. https://doi.org/10.1016/j.earscirev.2008.10.005

Dupraz, C., Visscher, P.T., Baumgartner, L.K. & Reid, R.P. (2004) Microbe-mineral interactions: early carbonate precipitation in a hypersaline lake (Eleuthera Island, Bahamas). *Sedimentology*, *51*, 745–765. https://doi.org/10.1111/j.1365-3091.2004.00649.x

Emeis, K.C., Richnow, H.H. & Kempe, S. (1987) Travertine formation in Plitvice National Park, Yugoslavia: chemical vs. biological control. *Sedimentology*, *34*(4), 595–609. https://doi.org/10.1111/j.1365-3091.1987.tb00789.x

Evans, C.S. (1933) Brisco-Dogtooth map area, British Columbia. Summary Report of the Geological Survey of Canada, Part A-2. Geological Survey of Canada, Ottawa, pp. 106–176. https://doi.org/10.4095/103129.

Fouke, B.W. (2011) Hot-spring systems geobiology: abiotic and biotic influences on travertine formation at Mammoth Hot Springs, Yellowstone National Park, USA. *Sedimentology*, *58*(1), 170–219. https://doi.org/10.1111/j.1365-3091.2010.01209.x

Fulton, R.J. (1971) Radiocarbon geochronology of southern British Columbia. Geological Survey of Canada, Paper 71–37, 28 p. https://doi.org/10.4095/102467.

Gabrielse, H. (1991). Structural styles. In: Gabrielse, H. & Yorath, C.J. (Eds.) *Geology of the Cordilleran Orogen in Canada*. Geology of Canada Series, volume 4; Geological Society of America, Geology of North America, Ottawa: Geological Survey of Canada, vol. *G-2*, pp. 571–675.

Gandin, A. & Capezzuoli, E. (2008) Travertine versus calcareous tufa: distinctive petrologic features and stable isotopes signatures. *Italian Journal of Quaternary Sciences*, *21*(1B), 125–136.

Gebauer, D., Völkel, A. & Cölfen, H. (2008) Stable prenucleation calcium carbonate clusters. *Science*, *322*, 1819–1822. https://doi.org/10.1126/science.1164271

Goodwin, A., Michel, F., Phillips, B., Keen, D., Dove, M. & Reeder, R. (2010) Nanoporous structure and medium-range order in synthetic amorphous calcium carbonate. *Chemistry of Materials*, *22*(10), 3197–3205. https://doi.org/10.1021/cm100294d

Grasby, S.E. & Hutcheon, I. (2001) Controls on the distribution of thermal springs in the southern Canadian Cordillera. *Canadian Journal of Earth Sciences*, *38*, 427–440. https://doi.org/10.1139/e00-091

Grasby, S.E., Hutcheon, I. & Krouse, H.R. (2000) The influence of water-rock interaction on the chemistry of thermal springs in western Canada. *Applied Geochemistry*, *15*(4), 439–454. https://doi.org/10.1016/S0883-2927(99)00066-9

Janissen, R., Murillo, D., Niza, B., Sahoo, P.K., Nobrega, M.M., Cesar, C.L., Temperini, M., Carvalho, H.F., de Souza, A.A. & Cotta, M.A. (2015) Spatiotemporal distribution of different extracellular polymetric substances and filamentation mediate *Xylella fastidiosa* adhesion and biofilm formation. *Scientific Reports*, *5*, 9856. https://doi.org/10.1038/srep09856

Jones, B. & Peng, X. (2012) Amorphous calcium carbonate associated with biofilms in hot springs. *Sedimentary Geology*, *269-270*, 58–68. https://doi.org/10.1016/j.sedgeo.2012.05.019

Jones, B. & Peng, X. (2014) Abiotic growth of needle-fiber calcite in Spring Towers at Shiqiang, Yunnan Province, China. *Journal of Sedimentary Research*, *84*(11), 1021–1040. https://doi.org/10.2110/jsr.2014.82

Jones, B. & Renaut, R.W. (2010) Calcareous spring deposits in continental settings. In Alonso-Zarza, A.M. & Tanner, L.H. (Eds.) *Developments in sedimentology: facies, environments, and processes*, Chapter 4. Amsterdam: Elsevier BV, vol. 61, pp. 177–224.

Kieser, W.E., Zhao, X-L., Clark, I.D., Cornett, R.J., Litherland, A.E., Klein, M., Mous, D.J.W. & Alary, J-F. (2015) The André E. Lalonde AMS Laboratory – the new acceleratory mass spectrometry facility at the University of Ottawa. *Nuclear Instruments and Methods in Physics, Research B*, *361*, 110–114. https://doi.org/10.1016/j.nimb.2015.03.014.

Kimura, T. & Koga, N. (2011) Monohydrocalcite in comparison with hydrated amorphous calcium carbonate: precipitation condition and thermal behavior. *Crystal Growth & Design*, *11*, 3877–3884. https://doi.org/10.1021/cg200412h

Knorre, H. & Krumbein, W. (2000) Bacterial calcification. In: Riding, R. & Awramik, S.M. (Eds.) *Microbial sediments*. Berlin: Springer, pp. 25–31.

Konhauser, K.O. (1997) Bacterial iron biomineralization in nature. *FEMS Microbiology Reviews*, *20*, 315–326. https://doi.org/10.1111/j.1574-6976.1997.tb00317.x

Konhauser, K.O. (1998) Diversity of bacterial iron mineralization. *Earth Science Reviews*, *43*, 91–121. https://doi.org/10.1016/S0012-8252(97)00036-6

Konhauser, K.O., Fyfe, W.S., Ferris, F.G. & Beveridge, T.J. (1993) Metal sorption and mineral precipitation by bacteria in two Amazonian river systems: Rio Solimoes and Rio Negro, Brazil. *Geology*, *21*, 1103–1106. https://doi.org/10.1130/0091-7613(1993)021<1103:MSAMPB>2.3.CO;2

Konrad, F., Purgstaller, B., Gallien, F., Mavromatis, V., Gane, P. & Dietzel, M. (2018) Influence of aqueous Mg concentration on the transformation of amorphous calcium carbonate. *Journal of Crystal Growth*, *498*, 381–390. https://doi.org/10.1016/j.jcrysgro.2018.07.018

Loste, E., Wilson, R., Seshadri, R. & Meldrum, F. (2003) The role of magnesium in stabilizing amorphous calcium carbonate and controlling calcite morphologies. *Journal of Crystal Growth*, *354*, 206–218. https://doi.org/10.1016/S0022-0248(03)01153-9

Lyu, J., Li, F., Zhang, C., Gower, L., Wasman, S., Sun, J., Yang, G., Chen, J., Gu, L., Tang, X. & Scheiffele, G. (2021) From the inside out: elemental compositions and mineral phases provide insights into bacterial calcification. *Chemical Geology*, *559*(5), 1197774. https://doi.org/10.1016/j.chemgeo.2020.119974

Lyu, J., Qin, W., Zhang, C. & Li, F. (2020) Nanoparticle accumulation in microbial induced carbonate precipitation: the crucial role

of extracellular polymeric substance. *Geomicrobiology Journal*, *37*(9), 837–847. https://doi.org/10.1080/01490451.2020.1786866

Mann, S., Heywood, B.R., Rajam, S. & Birchall, J.D. (1988) Controlled crystallization of CaCO3 under stearic acid monolayers. *Nature*, *334*, 692–695. https://doi.org/10.1038/334692a0

Mass, T., Giuffre, A., Sun, C., Stifler, C., Frazier, M., Neder, M., Tamura, N., Stan, C., Marcus, M. & Gilbert, P. (2017) Amorphous calcium carbonate particles form coral skeletons. *Proceedings of the National Academy of Sciences of the USA*, *114*, 1–9. https://doi.org/10.1073/pnas.1707890114

Meldrum, F.C. (2003) Calcium carbonate in biomineralisation and biomimetic chemistry. *International Materials Review*, *48*(3), 187–224. https://doi.org/10.1179/095066003225005836

Nehrke, G. & Cappellen, P.V. (2006) Framboidal vaterite aggregates and their transformation into calcite: a morphological study. *Journal of Crystal Growth*, *287*(2), 528–530. https://doi.org/10.1016/j.jcrysgro.2005.11.080

Nishiyama, R., Munemoto, T. & Fukushi, K. (2013) Formation condition of monohydrocalcite from $CaCl_2$-$MgCl_2$-Na_2Co solutions. *Geochimica et Cosmochimica Acta*, *100*, 2178–2231. https://doi.org/10.1016/j.gca.2012.09.002

Obst, M., Dynes, J., Lawrence, J., Swerhone, G., Benzerara, K., Karunakaran, C., Kaznatcheev, K., Tyliszczak, T. & Hitchcock, A. (2009) Precipitation of amorphous $CaCO_3$ (aragonite-like) by cyanobacteria: a STXM study of the influence of EPS on the nucleation process. *Geochimica et Cosmochima Acta*, *73*(14), 4180–4198. https://doi.org/10.1016/j.gca.2009.04.013

Ogino, T., Suzuki, T. & Sawada, K. (1987) The formation and transformation mechanism of calcium carbonate in water. *Geochimica et Cosmochimica Acta*, *51*(10), 2757–27667. https://doi.org/10.1016/0016-7037(87)90155-4

Osborn, G. & Luckman, B.H. (1988) Holocene glacial fluctuations in the Canadian Cordillera (Alberta and British Columbia). *Quaternary Science Reviews*, *7*(2), 115–128. https://doi.org/10.1016/0277-3791(88)90002-9

Owen, R.B., Renaut, R.W. & Stamatakis, M.G. (2010) Diatomaceous sedimentation in late Neogene lacustrine basins of western Macedonia, Greece. *Journal of Paleolimnology*, *44*, 343–359. https://doi.org/10.1007/s10933-010-9409-5

Pan, J., Zhao, H., Tucker, M., Zhou, J., Jiang, M., Wang, Y., Zhao, Y., Sun, B., Han, Z. & Yan, H. (2019) Biomineralization of monohydrocalcite induced by the Halophile *Halomanas Smyrnensis* WMS-3. *Minerals*, *9*(10), 632. https://doi.org/10.3390/min9100632

Pedley, H.M. (1990) Classification and environmental models of cool freshwater tufas. *Sedimentary Geology*, *68*, 143–154. https://doi.org/10.1016/0037-0738(90)90124-C

Peng, X. & Jones, B. (2013) Patterns of biomediated $CaCO_3$ crystal brushes in hot spring deposits. *Sedimentary Geology*, *294*, 105–117. https://doi.org/10.1016/j.sedgeo.2013.05.009

Perri, E., Manzo, E. & Tucker, M. (2012) Multi-scale study of the role of biofilm in the formation of minerals and fabrics in calcareous tufa. *Sedimentary Geology*, *263-264*, 16–29. https://doi.org/10.1016/j.sedgeo.2011.10.003

Perri, E., Slowakiewicz, M., Perrotta, I. & Tucker, M. (2021) Biomineralization processes in modern calcareous tufa: possible roles of viruses, vesicles and extracellular polymeric substances (Corvino Valley – Southern Italy). *Sedimentology*, *69*(2), 399–422. https://doi.org/10.1111/sed.12932

Politi, Y., Arad, T., Klein, E., Weiner, S. & Addadi, L. (2004) Sea urchin spine calcite forms via a transient amorphous calcium carbonate phase. *Science*, *306*(5699), 1161–1164. https://doi.org/10.1126/science.1102289

Qin, W., Wang, C., Ma, Y., Shen, M., Li, J., Jiao, K., Tay, F. & Niy, L. (2020) Microbe-mediated extracellular and intracellular mineralization: environmental, industrial, and biotechnical applications. *Advanced Materials*, *32*, 1907833. https://doi.org/10.1002/adma.201907833

Radha, A.V., Forbes, T.Z., Killian, C.E., Gilbert, P.U. & Navrotsky, A. (2010) Transformation and crystallization energies of synthetic and biogenic amorphous calcium carbonate. *Proceedings of the Natural Academy of Sciences*, *107*(38), 16438–16443. https://doi.org/10.1073/pnas.1009959107

Rainey, D.K. (2009) Rocky Mountain carbonate spring deposit development. PhD Dissertation, University of Alberta, Edmonton, 212 p.

Rainey, D.K. & Jones, B. (2007) Rapid cold water formation and recrystallization of relict bryophyte tufa at the Fall Creek cold springs, Alberta, Canada. *Canadian Journal of Earth Sciences*, *44*(7), 889–909. https://doi.org/10.1139/e07-008

Rainey, D.K. & Jones, B. (2009) Abiotic versus biotic controls on the development of the Fairmont Hot Springs carbonate spring deposit, British Columbia, Canada. *Sedimentology*, *56*(6), 1832–1857. https://doi.org/10.1111/j.1365-3091.2009.01059.x

Rainey, D.K. & Jones, B. (2010) Preferential soft-tissue preservation in the Hot Creek carbonate spring deposit, British Columbia, Canada. *Sedimentary Geology*, *227*(1), 20–36. https://doi.org/10.1016/j.sedgeo.2010.03.003

Reimer, P. et al. (2020) The IntCal20 Northern hemisphere radiocarbon age calibration curve (0-55 cal kBP). *Radiocarbon*, *62*(4), 725–757. https://doi.org/10.1017/RDC.2020.41

Reimer, P.J., Brown, T.A. & Reimer, R.W. (2004) Discussion: reporting and calibration of post-bomb ^{14}C data. *Radiocarbon*, *46*(3), 1299–1304. https://doi.org/10.1017/S0033822200033154

Reitner, J., Arp, G., Thiel, V., Gautret, P., Galling, U. & Michaelis, W. (1997) Organic matter in Great Salt Lake ooids (Utah, USA): first approach to a formation via organic matrices. *Facies*, *36*, 210–219.

Rez, P., Sinha, S. & Gal, A. (2014) Nanocrystallite model for amorphous calcium carbonate. *Journal of Applied Crystallography*, *47*(5), 1651–1657. https://doi.org/10.1107/S1600576714018202

Riding, R. (2000) Microbial carbonates: the geological record of calcified bacterial–algal mats and biofilms. *Sedimentology*, *47*, 179–214. https://doi.org/10.1046/j.1365-3091.2000.00003.x

Robin, N., Bernard, S., Miot, J., Blanc-Valleron, M., Charbonnier, S. & Petit, G. (2015) Calcification and diagenesis of bacterial colonies. *Minerals*, *5*, 488–506. https://doi.org/10.3390/min5030488

Rodriguez-Blanco, J.D., Shaw, S. & Benning, L.G. (2011) The kinetics and mechanisms of amorphous calcium carbonate (ACC) crystallization to calcite, via vaterite. *Nanoscale*, *3*, 265–271. https://doi.org/10.1039/C0NR00589D

Rodriguez-Blanco, J.D., Shaw, S. & Benning, L.G. (2015) A route for the direct crystallization of dolomite. *American Mineralogist*, *100*, 1172–1181. https://doi.org/10.2138/am-2015-4963

Rodriguez-Blanco, J.D., Shaw, S., Bots, P., Roncal-Herreo, T. & Benning, L. (2014) The role of Mg in the crystallization of monohydrocalcite. *Geochemica et Cosmochimica Acta*, *127*, 204–220. https://doi.org/10.1016/j.gca.2013.11.034

Rodriguez-Navarro, C., Jimenez-Lopez, C., Rodriguez-Navarro, A., Gonzalez-Muñoz, M. & Rodriguez-Gallego, M. (2007) Bacterially mediated mineralization of vaterite. *Geochmica et Cosmochimica Acta*, *71*(5), 1197–1213. https://doi.org/10.1016/j.gca.2006.11.031

Rodriquez-Blanco, J.D., Shaw, S., Bots, P., Roncal-Herrero, T. & Benning, L.G. (2012) The role of pH and Mg on the stability and crystallization of amorphous calcium carbonate. *Journal of Alloys and Compounds*, *536*, S477–S479. https://doi.org/10.1016/j.jallcom.2011.11.057

Schmidt, M.P., Ilott, A.J., Phillips, B.L. & Reeder, R.J. (2014) Structural changes upon dehydration of amorphous calcium carbonate. *Crystal Growth & Design*, *14*(3), 938–951. https://doi.org/10.1021/cg401073n

Shen, Q., Wei, H., Zhou, Y., Huang, Y., Yang, H., Wang, D. & Xu, D. (2006) Properties of amorphous calcium carbonate and the template action of vaterite spheres. *Journal of Physical Chemistry B*, *110*, 2994–3000. https://doi.org/10.1021/jp055063o

St-Jean, K., Kieser, W.E., Crann, C.A. & Murseli, S. (2017) Semi-automated equipment for CO2 purification and graphitization at the A. E. Lalonde AMS Laboratory (Canada). *Radiocarbon*, *59*(3), 941–945. https://doi.org/10.1017/RDC.2016.57

Stuiver, M. & Polach, H.A. (1977) Discussion: reporting of ^{14}C data. *Radiocarbon*, *19*(3), 355–363. https://doi.org/10.1017/S0033822200003672

Swainson, I.P. (2008) The structure of monohydrocalcite and the phase composition of the beachrock deposits of Lake Butler and Lake Fellmongery, South Australia. *American Mineralogist*, *93*, 1014–1018. https://doi.org/10.2138/am.2008.2825

Turner, E.C. & Jones, B. (2005) Microscopic calcite dendrites in cold-water tufa: implications for nucleation of micrite and cement. *Sedimentology*, *52*, 1043–1066. https://doi.org/10.1111/j.1365-3091.2005.00741.x

Verrecchia, E. & Verrecchia, K. (1994) Needle-fiber calcite: a critical review and a proposed classification. *Journal of Sedimentary Research*, *64A*(3), 650–664.

Wang, Y.-Y., Yao, Q.-Z., Zhou, G.-T. & Fu, S.-Q. (2015) Transformation of amorphous calcium carbonate into monohydrocalcite in aqueous solution: a biomimetic mineralization study. *European Journal of Mineralogy*, *27*, 717–729. https://doi.org/10.1127/ejm/2015/0027-2486

Weiner, S., Levi-Kalisman, Y., Raz, S. & Addadi, L. (2003) Biologically formed amorphous calcium carbonate. *Connective Tissue Research*, *44*(1), 214–218. https://doi.org/10.1080/03008200390181681

Xu, X., Han, J.T. & Cho, K. (2004) Formation of amorphous calcium carbonate thin films and their role in biomineralization. *Chemistry of Materials*, *16*(9), 1740–1746. https://doi.org/10.1021/cm035183d

Zavarin, G.A. (2002) Microbial geochemical calcium cycle. *Microbiology*, *71*, 5–22. https://doi.org/10.1023/A:1017945329951

How to cite this article: Broughton, P. L. (2022) Microbial EPS-mediated amorphous calcium carbonate–monohydrocalcite–calcite transformations during early tufa deposition. *The Depositional Record*, *00*, 1–28. https://doi.org/10.1002/dep2.200